A SMALL SCALE MAGNETIC PARTICLE RELAXOMETER

A Thesis

by

AHMED TAREK MOHAMED ALY EL GHAMRAWY

Submitted to the Office of Graduate and Professional Studies of
Texas A&M University
in partial fulfillment of the requirements for the degree of

MASTER OF SCIENCE

Chair of Committee,	Steven M. Wright
Committee Members,	Mary P. McDougall
	Erchin Serpedin
	Jim X. Ji
Head of Department,	Chanan Singh

December 2013

Major Subject: Electrical Engineering

ABSTRACT

Magnetic Particle Imaging (MPI) is a newly found imaging modality. It utilizes superparamagnetic materials as tracers in the blood stream to obtain very high resolutions. MPI promises to have high sensitivity, high spatial resolution and no radiation compared to other imaging modalities. Most commercially available MRI tracers (used for MPI for now) are all non-harmful when compared to Iodine (used for CT scan) and Gadolinium (used for MRI). MPI research is divided into three categories: MPI scanner development, superparamagnetic materials development, and image reconstruction techniques. In this project a small scale LabView-based system will be developed for use on small lab created phantoms, using 25 nm superparamagnetic iron oxide (SPIO) particles. At first a relaxometer will be developed, the imager will come as the next step. Transmitting and receiving signals will be implemented using LabView and a National Instruments PXI-1033 Chassis. Lab-built coils will be used to send the excitation signal and receive the signal induced by those SPIO's.

The objective of this project is to be introduced to a new imaging modality that can have various applications and at the same time considered safe. The system being built is considered inexpensive and shows most of the aspects of how magnetic particle imaging works, starting with the physical phenomena, superparamagnetic nanoparticle properties and relaxation, signal generation and acquisition, and an introduction to the hardware of MPI. The system can be used to introduce engineers and engineering students to the MPI physical phenomena.

ACKNOWLEDGEMENTS

I would like to thank my committee chair, Dr. Steven Wright, for his guidance, patience and introducing me to biomedical imaging research. I would also like to thank my committee members, Dr. Mary McDougall, Dr. Jim Ji, and Dr. Erchin Serpedin. Thanks also go to Dr. John Bosshard and my colleagues at MRSL for their knowledge and help.

I am particularly grateful for the opportunity given by my sponsor, Qatar Foundation-Research Division to complete my masters here at Texas A&M University.

Special thanks to my family and friends for their constant support, encouragement. I would like to express my very great appreciation to my mother, who has been my source of comfort and inspiration. Finally, I praise Allah, the almighty for granting me the ability to proceed successfully.

NOMENCLATURE

MPI	Magnetic Particle Imaging
CT	Computed Tomography
MRI	Magnetic Resonance Imaging
SPIO	Superparamagnetic Iron Oxide
DF	Drive Field
PA	Power Amplifier
LNA	Low Noise Amplifier
ADC	Analog to Digital
AWG	American Wire Gauge
Q	Quality Factor
SNR	Signal to Noise
PSF	Point Spread Function
FWHM	Full Width Half Maximum
FFP	Field Free Point
FOV	Field of View
FFL	Field Free Line
SAR	Specific Absorption Rate
CKD	Chronic Kidney Disease

TABLE OF CONTENTS

Page

LIST OF FIGURES

Page

LIST OF TABLES

Page

CHAPTER I

INTRODUCTION

I.1. Magnetic Particle Imaging

Magnetic Particle Imaging (MPI) is a newly found tomographic imaging modality [1]. It utilizes superparamagnetic nanoparticles (generally iron oxide) as tracers in the blood stream to obtain very high resolution images, in addition to real time imaging. MPI promises to have high sensitivity, high spatial resolution and no radiation concerns compared to other imaging modalities. Most commercially available MRI tracers (used for MPI for now) are all non-harmful when compared to Iodine (used for CT scan) and Gadolinium (used for MRI). Many studies have reached the result that iodine-based media used in angiography have led to kidney dysfunction [2]. In 2008, the first *in vivo* 3D real-time MPI scans of a beating mouse heart were presented using a clinically approved concentration of a commercially available MRI contrast agent at Philips Research [3]. With these capabilities, MPI has potential to become a leading imaging application. MPI research is divided into three categories: MPI scanner development, image reconstruction techniques and superparamagnetic nanoparticles development.

I.2. MPI Physical Phenomena

MPI utilizes the non-linear response of superparamagnetic nanoparticles and nanoparticle magnetic saturation at specific magnetic fields. Using a varying magnetic field (Drive Field) at a specific frequency (f_0) with sufficient amplitude causes the

magnetization of the nanoparticles to periodically change between a maximum and a minimum. Nanoparticles experiencing constant maximum and minimum values of magnetization are said to be in saturation. The combination of the non-linear response and the drive field could be expressed using a Fourier transform. As a result of the non-linear relationship the particle signal has not only a peak at the fundamental frequency, f_0, but at all higher harmonics [1].

In Figure I-1a, applying a varying magnetic field (green) in the non-linear part where the magnetization (black) changes between a maximum and a minimum induces the non-linear response (red). The Fourier transform shows how the induced signal is represented in harmonics. In Figure I-1b, applying a varying magnetic field in the saturation region does not utilize the non-linear response of the particles. As a result, the induced harmonics from the particles is very low [1].

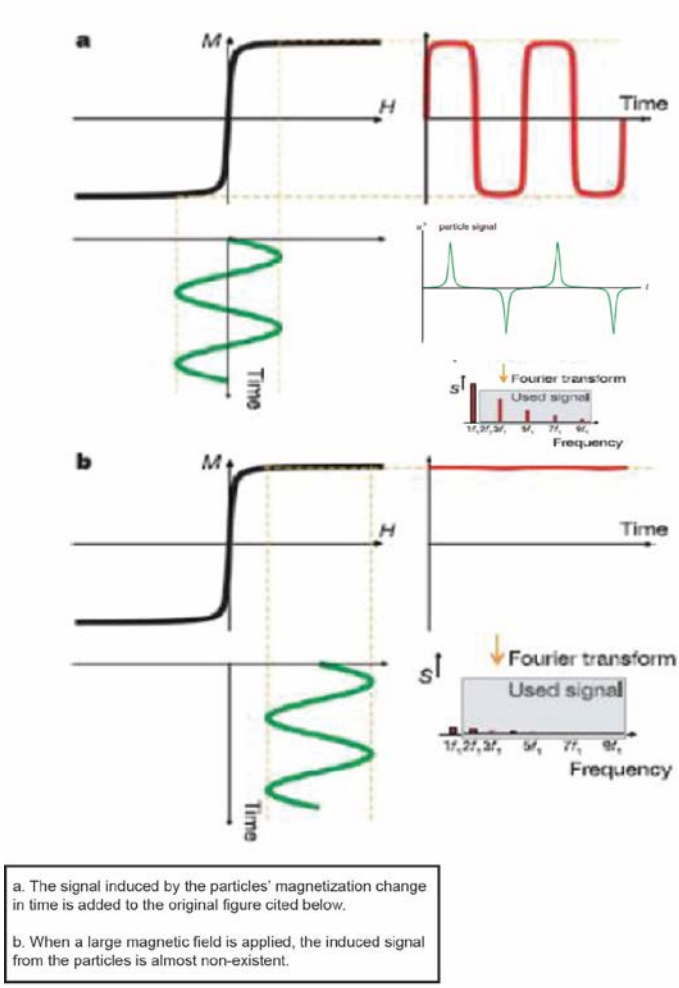

a. The signal induced by the particles' magnetization change in time is added to the original figure cited below.

b. When a large magnetic field is applied, the induced signal from the particles is almost non-existent.

Figure II-1 a. Response of iron oxide particle magnetization to an external varying magnetic field. b. Response of iron oxide particle magnetization to an external constant magnetic field is added to the varying magnetic field [1].

I.3. Superparamagnetic Iron Oxide Particles

The main objective of an MPI imager is to be able to locate the superparamagnetic nanoparticles concentration in space. MPI has higher sensitivity than MRI because the magnetic moment of iron oxide nanoparticles is eight orders of magnitude larger than the proton magnetic moment used in MRI [4]. Iron oxide material

in the form of nanoparticles is used widely in MPI. Nanoparticles are made of two layers, a superparamagnetic core responsible for the magnetic response of the particle and a magnetic neutral coating which prevents particle agglomeration. The larger the coating, less particle-particle interaction is experienced. Dextran, a polysaccharide based on glucose molecules, is water soluble and has shown excellent results in being safe and biocompatible [5].

Each nanoparticle magnetization is represented with a magnetization vector. The magnetization vector will be following the direction of varying drive field. If a constant field is used the magnetization vector of the particles will follow in the same direction. Increasing the amplitude of the constant field increases the number of particles aligned with the constant field. The particle response can be divided into a dynamic part and the saturation part. Dynamic part is caused by a varying field. Saturation is caused by a constant magnetic field. The relation between particle magnetization and the external magnetic field depends on the size of the iron core. In Figure I-2, we can see that for particles with 30 nm diameter, an external magnetic field (H) of 5 $mT\mu_0^{-1}$ puts the particle in saturation. Between -5 and 5 $mT\mu_0^{-1}$ puts the particle in the dynamic range [6]. The units $mT\mu_0^{-1}$ was first introduced in Bernhard Gleich and Jürgen Weizenecker Nature paper and has been used in all MPI publications to present magnetic field strengths on a tesla scale. The positive and negative values indicate the direction of the magnetic field.

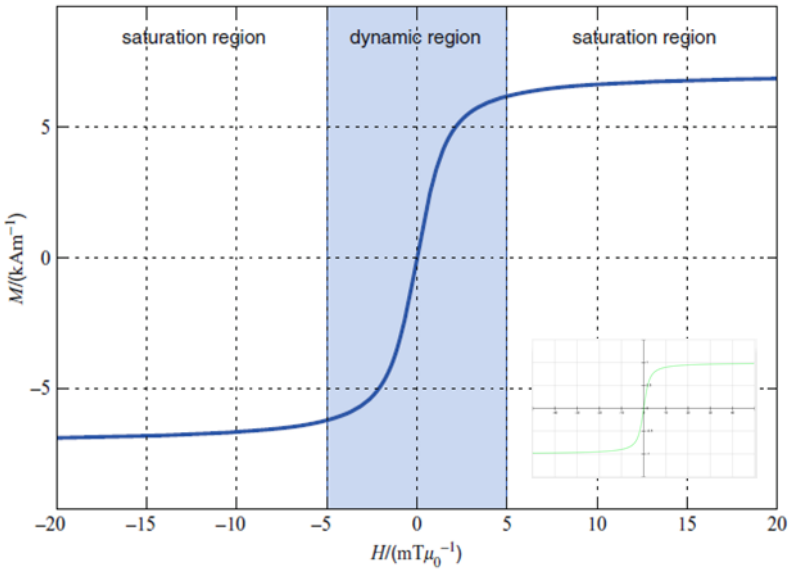

Figure I-2 Response of 30 nm iron oxide particle magnetization to external magnetic field with the Langevin function placed in the bottom right corner [6].

The response of the particles magnetization can be described using the Langevin function given in equation 1. The Langevin function (equation 2) is a representation of the magnetization curve shown earlier in Figure I-2. As ξ increases the particle gets closer to being in saturation. At ξ = 0, the particle has zero magnetization i.e. experiences no external magnetic field.

$$M(H) = c\, m\, \mathcal{L}(\beta H) \tag{1}$$

$$\mathcal{L}(\xi) = \begin{cases} (\coth\ (\xi) - \frac{1}{\xi} & \xi \neq 0 \\ 0 & \xi = 0 \end{cases} \tag{2}$$

with

$$\beta = \frac{\mu_0 m}{k_B T^P} \tag{3}$$

Here, k_B denotes the Boltzmann constant, T^P denotes the particle temperature, μ_0 denotes permeability of free space and m denotes the modulus of the magnetic moment of a single particle. In equation 1, the particle concentration (amount of particles) c and the particle magnetic moment m are multiplied by the Langevin function, H is the applied varying magnetic field, equation 4 shows how m is calculated:

$$m = V\, M_{CORE}^{S} \;,\; V = \frac{\pi D^3}{6} \tag{4}$$

M_{CORE}^{S} is saturation magnetization of the material of the particle, it's a property of the material in our case its iron oxide. V is the volume of the iron core of the particle. D is the diameter of the iron core. From equation 1 and 4, keeping the total iron concentration or the total amount of iron constant, we can deduce that the magnetization is dependent on particle iron core size.

Ideally, for the iron oxide nanoparticles to reach full saturation, an infinite external constant magnetic field has to be applied. Therefore, we consider that the particles are in saturation when 80 percent of the particles are saturated. The Langevin function $\mathcal{L}(\beta H^S) = 0.8$ when the particles are 80 percent saturated. We obtain a value of 0.8 when $\xi = 5$ from equation 2. $\beta H^S = 5$. H^S is denoted with an S for saturation. In equation 5, H^S is calculated showing its inverse relationship with particle diameter size.

This means particles with smaller iron core diameters require more external magnetic fields to reach saturation. Figure I-3 shows magnetization of the particles change with changing iron core diameters while keeping iron concentration constant [6].

$$H^S = \frac{5}{\beta} = \frac{5k_BT^P}{\mu_0\, m} = \frac{5k_BT^P}{\mu_0\, V\, M_{CORE}^S} \tag{5}$$

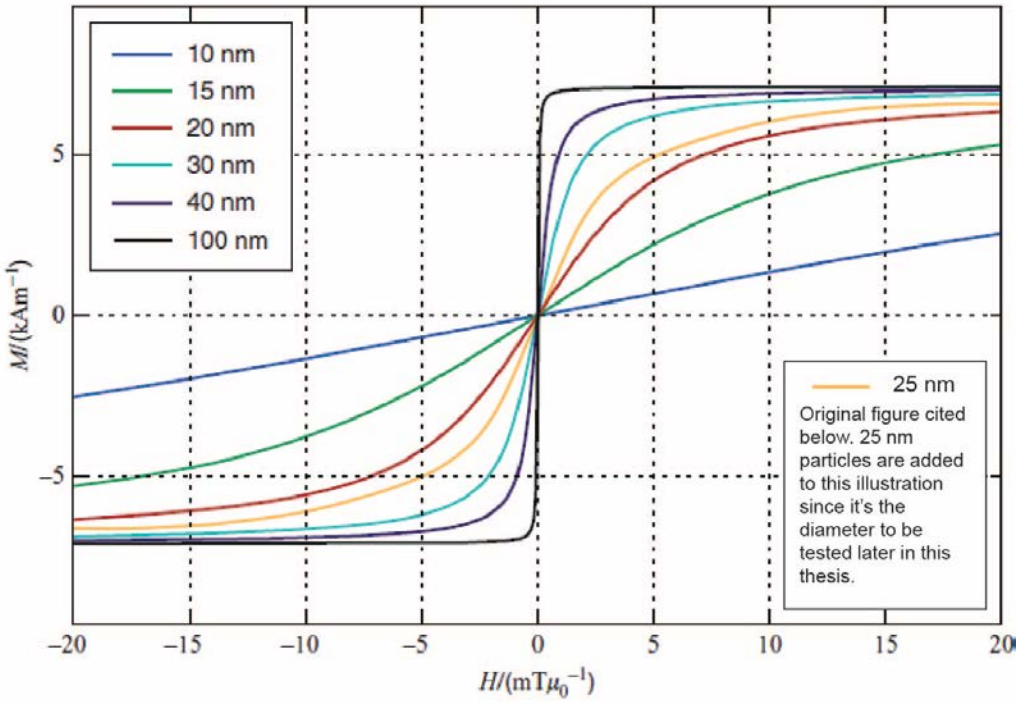

Figure I-3 Response of iron oxide particle magnetization to external magnetic field for different particle diameters [6].

The last aspect of the nanoparticles to be discussed is its relaxation. As mentioned earlier the particle's magnetization vector will be following the varying magnetic field. The frequency of this field affects the relaxation time greatly. In simple

terms the applied frequency controls the rate of which the magnetization of the particles change, at lower frequencies the magnetization of the particles can follow the change in the drive field. Meanwhile, at higher frequencies the magnetization of the particles may not be able to follow and loose most of the amplitude. In general the excitation frequency should be very small in value in comparison to the reciprocal of the relaxation time of the particles [6].

When a single domain nanoparticle suspended in a fluid is exposed to an external magnetic field, its magnetic moment rotation can be characterized using two types of motion: Brownian and Néel motion. Brownian motion is described as the whole particle physically rotating in the fluid. Néel motion is described as the magnetic moment direction rotates within the particle without the particle physically moving. Brownian motion and Néel motion relaxation times are calculated using equation 6 and equation 7 below. Calculating these relaxation times in an experimental setting involves applying a constant external magnetic field and turning it off [7-10].

$$\tau_B = \frac{3\,\eta\,V_H}{k_B T^P} \tag{6}$$

$$\tau_N = \tau_0 \exp\left(\frac{K^A V}{k_B T^P}\right) \tag{7}$$

From equation 6 and 7, V_H is the hydrodynamic volume of the particle, η is the viscosity of the fluid, τ_0 is a fixed time being a characteristic of the material and it is approximated to be 10^{-9} s. K^A is the anisotropic energy constant and V is the particle core volume. In

general both types of motion play a role in determining the overall relaxation of the particles τ_{eff} shown in equation 8, making the smaller relaxation time dominating the total relaxation.

$$\tau_{eff} = \frac{\tau_B \tau_N}{\tau_B + \tau_N} \tag{8}$$

From the equation 6 and 7, we can conclude that Brownian motion relaxation time depends on the viscosity and the hydrodynamic volume and the Néel motion relaxation depends exponentially on the iron core volume. So both Brownian and Néel motion relaxation time increases with increasing the particle size. The larger the diameter, the steeper is the rise in the magnetization curve harmonics can be detected before the signal reaches noise level. Moreover, at higher frequencies physical movement of the particles takes longer time, thus making Néel motion relaxation time shorter and therefore more dominant. In short, Brownian motion dominates in viscous fluids and in lower frequencies and Néel motion dominates in higher frequencies and higher magnetic fields. As magnetic anisotropy and relaxation reduce the induced signal as particle diameter increases, particles with diameter between 20 and 30 nm are considered to be the best for MPI [4, 6-11].

I.4. Magnetic Particle Relaxometer

Building a relaxometer provides the user with very important information about the nanoparticles that will be used. Brownian and Néel relaxation delays the nanoparticles' response to the external magnetic field. This delay can vastly affect the quality of the image produced later. Increasing the particle core diameter theoretically would increase the received nanoparticle signal and as a result, increasing image quality but only if relaxation is kept constant. A relaxometer helps give us an idea about different particle relaxation trends depending on diameter, excitation frequency and other factors. The conclusion we acquire will later help us choose the best nanoparticles for imaging purposes [4, 6-11].

CHAPTER II

MPI HARDWARE

II.1. MPI System Implementation

As mentioned before, MPI utilizes the non-linear response of superparamagnetic nanoparticles and nanoparticle magnetic saturation at specific magnetic fields. The Drive Field (DF) causes nanoparticle excitation with sufficient amplitude at a certain frequency (f_0). The DF will be obtained using an excitation coil. A signal generator will be used to generate a sinusoidal signal representing the varying magnetic field required for particle excitation. A power amplifier (PA), getting its field from the signal generator, will be used to power up the excitation coil.

After the nanoparticles are excited, the signal that is induced by the particles is picked up using a receiver coil. The signal coming from the receiver coil will be amplified using a low noise amplifier (LNA) to assist detecting the weaker nanoparticle signal. The amplitude of the harmonics produced by the nanoparticle excitation is small in value when compared to the DF amplitude [12].

The signal is picked up by an Analog to Digital Converter (ADC) for further processing of the signal including Fourier analysis. The National Instruments PXI-1033 chassis includes two cards one will be used to generate the sinusoid for particle excitation and the other used as an ADC. The block diagram in Figure II-1 shows the flow of the signal starting at the signal generator and ending at the ADC where the nanoparticle signal is captured. You also have to note that the receiver coil is set

coaxially inside the excitation coil. The nanoparticles will be placed in the center on the receiver coil.

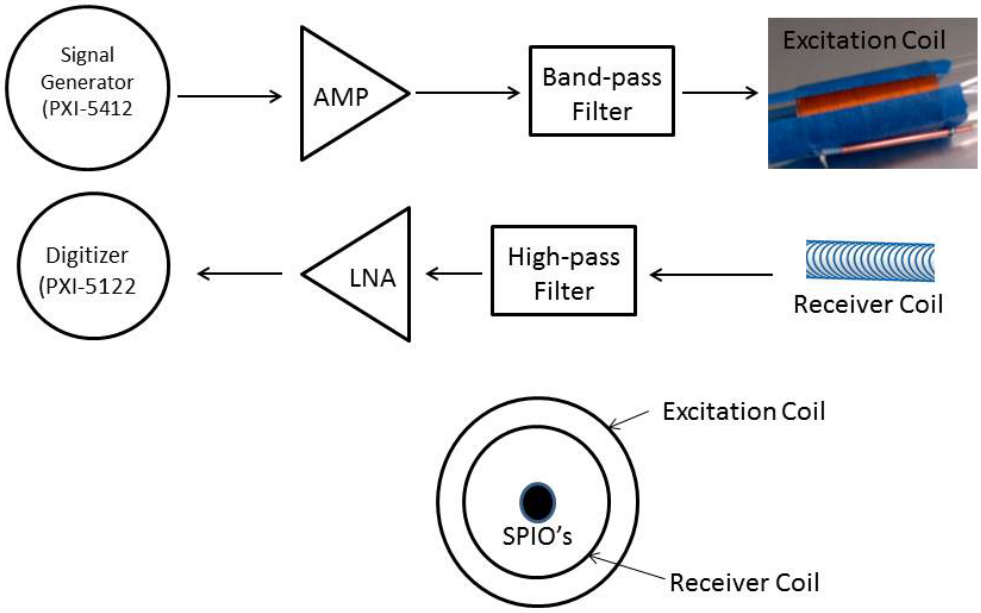

Figure II-1 Magnetic Particle Relaxometer system block diagram.

II.2. Hardware Outline

- PXI-1033 Chassis: Controlled by National Instruments (NI) LabView system design software. The chassis includes two cards that will be used:
    - NI PXI-5412: 100 MS/s, 14 bit arbitrary waveform generator used to generate excitation sinusoid at $f_0 = 100$ kHz.

    - NI PXI-5122: 100 MS/s, 14 bit arbitrary digitizer used as an ADC.

- LZY-22+: PA by Mini circuits, outputs 30 W with a frequency range from 100 kHz to 200 MHz.
- Band-pass Filter: a lab-built filter centered around 100 kHz to ensure signal feed to excitation coil is clean with no unwanted harmonics.
- Excitation Coil: simple solenoid made of 60 windings, 4.4 cm length and a 1 cm radius.
- Receiver Coil: a solenoid placed coaxially in the center of the excitation coil made of 30 windings, 1.1 cm length and a 0.4 cm length.
- ZFHP-0R23: a high-pass filter, passband frequency greater than 230 kHz, used to filter the excitation signal at f_0 (100 kHz) after receiver coil.
- AU1647: LNA by Miteq, 57 dB gain and frequency range 100kHz to 400 MHz. Used to amplify
- NI PXI-5122: 100 MS/s, 14 bit arbitrary digitizer used as an ADC.
- 25 nm SPIO's: manufactured by Ocean Nanotech, they are water soluble iron oxide nanoparticles with amphiphilic polymer coating. 2 mL were purchased with 5 mg/mL concentration.

II.3. System Requirements

II.3.1 Preparing PA Input

There are certain system requirements that had to be met before all the hardware was assembled together. The first simple requirement is to make sure the signal generator does not exceed the input power rating of the PA. The PA maximum input power allowed is 20 dBm. LabView program controls the 5412 card and allows you to pick signal amplitude, signal type and shape (constant or varying), signal frequency and duration of the signal. Signal amplitude ranges from 0 to 1 and it represents the power output. A simple way to test the card's output is to hook the 5412 card to an Agilent Technologies DSO3062A oscilloscope through a T connector with 50 ohms. All system components impedance should be 50 ohms. In Table II.1, the power output from the 5412 card is calculated for various amplitudes. The table consists of the amplitude of the signal from the 5412 card, the peak to peak voltage, the power output in watts and dBm. At 0.99 amplitude, the power output is around 10 dBm, which does not exceed 20 dBm, so using maximum amplitude from the 5412 card is acceptable and would not damage the PA.

Table II.1 Power output of PXI-5412 card at 50 ohms.

AMP	Vpp (mV)	Power (mW)	Power (dBm)
0.1	208	0.10816	-9.659333214
0.2	400	0.4	-3.979400087
0.3	592	0.87616	-0.574165779
0.4	784	1.53664	1.86572134
0.5	976	2.38144	3.76839644
0.6	1168	3.41056	5.328256942
0.7	1360	4.624	6.650178254
0.8	1552	6.02176	7.797234425
0.9	1744	7.60384	8.810329699
0.99	1936	9.37024	9.717507146

II.3.2 Building Excitation Coil

The coil was built by winding laminated 30 AWG copper wire around a plexiglass tube of diameter 2 cm. The coil is shown in Figure II-2.

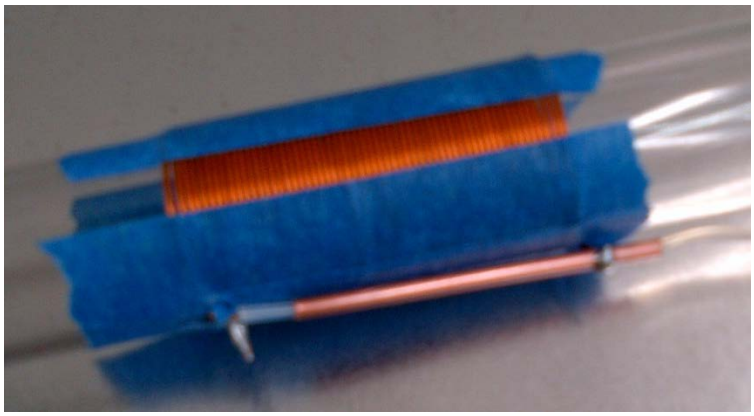

Figure II-2 Excitation coil.

As mentioned all system components have to have an impedance of 50 ohms. As a result, the lab-built excitation coil has to be impedance matched to 50 ohms and tuning frequency (f_0 = 100 kHz) using a matching circuit. A matching circuit is used to make sure maximum power is transferred from the source to a load and to protect the system from reflected power. To find the required capacitance values for matching, we need to calculate excitation coil resistance (R) and inductance (L). Both valued were measured using a BK Precision 885 LCR meter. The inductance of a solenoid can also be calculated using equation 9 below.

$$L = \frac{\mu_0 N^2 \pi r^2}{l} \tag{9}$$

μ_0 denotes the permeability of free space, N denotes the number of turns of the excitation coil, l is the coil length and r is the radius of the coil. The measured values were R = 1.1 ohm and L = 33 μF. In Figure II-3 below, we have C1, capacitor that transforms coil impedance to 50 ohms, and C2, capacitor that cancels remaining reactance. Z_L is total load impedance in our case, load is excitation coil. Z_L contains both coil resistance 1.1 ohms and coil reactance (X_L=j2πL) j20.37 ohms. Equation 10 and 11 shows how both C1 and C2 are calculated.

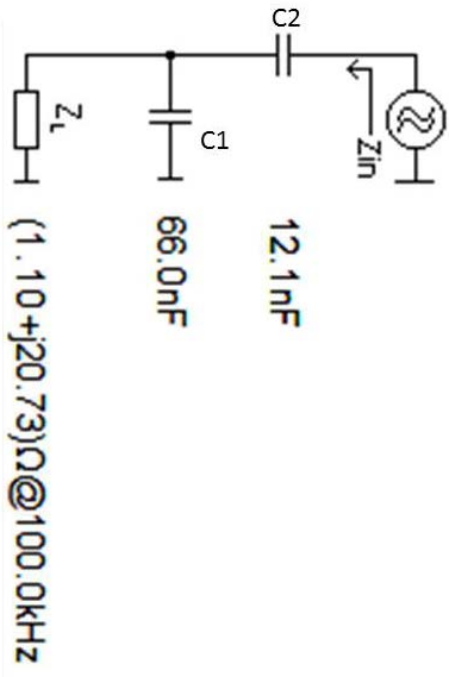

Figure II-3 Excitation coil matching circuit diagram.

$$Re\left(\frac{1}{j\omega C1+\frac{1}{R_L+j\omega L}}\right)=50 \tag{10}$$

Plugging in the resistance and the inductance and solving for C1, you will get two values for C1: 66 nF and 87 nF. In equation 11 below, you have to equate the imaginary part to C2. Plugging 66 nF in the imaginary part results in a positive reactance and therefore a capacitance value. Plugging in 87 nF results in a negative reactance and therefore an inductance value and we want a matching circuit consisting of capacitors.

$$Im\left(\frac{1}{j\omega*66*10^{-9}+\frac{1}{R_L+j\omega L}}\right)=131,\quad \frac{1}{j\omega C2}=-j*131,\quad C2=\frac{1}{\omega*131}=12\,nF \tag{11}$$

II.3.3 DF Magnetic Field Strength

The next requirement is to make sure the amplifier feeds a sufficient amount of power to the coil for the nanoparticles to be excited. Going back to Figure I-3 we can see that a DF in the region of 10 $mT\mu_0^{-1}$ will be enough to cause the nanoparticles of 25 nm to change magnetization across most of its dynamic range. The particles will be placed in the center of the excitation coil. Magnetic field at the center of the excitation coil is considered to be homogenous. Equation 12 below, shows to calculate the required DF (H(t)) [12].

$$H(t) = \frac{N}{2\sqrt{\left(\frac{l}{2}\right)^2 + r^2}}\, i(t) \tag{12}$$

N denotes the number of turns of the excitation coil, l is the coil length, r is the radius of the coil and i(t) is the current through the coil. The setup, in Figure II-4, is similar for testing the output of the 5412 card but in this case we will be adding a 30 dB attenuator before the oscilloscope to protect the oscilloscope from the PA's high power. Also a T connector with 50 ohms is used to simulate a 50 ohm system.

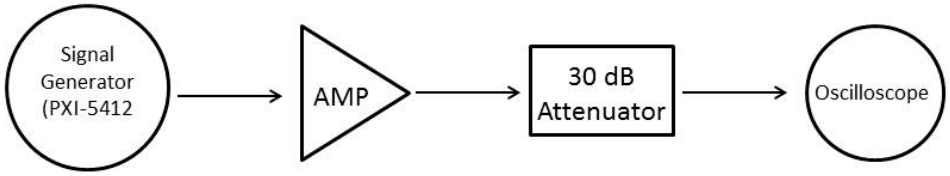

Figure II-4 PA output power test setup block diagram.

In Table II-2 below, we will have like the last table the amplitude of the signal from the5412 card, the peak to peak voltage, the power output in watts and dBm, and gain. The gain in this case is the setup gain, it has a low value due to the attenuator in place, but the real PA gain will be that gain value at specific amplitude plus 30 dB.

Table II.2 PA output power test setup values at 50 ohm.

AMP	Vpp (mV)	Power (W)	Power (dBm)	Gain
0.1	1281	4.1024025	6.130382682	15.78972
0.2	2361	13.9358025	11.44131983	15.42072
0.3	2721	18.5096025	12.67397092	13.24814
0.4	2921	21.3306025	13.29003123	11.42431
0.5	3041	23.1192025	13.63972849	9.871332
0.6	3241	26.2602025	14.19298071	8.864724
0.7	3201	25.6160025	14.08511357	7.434935
0.8	3361	28.2408025	14.50877034	6.711536
0.9	3321	27.5726025	14.4047776	5.594448
0.99	3361	28.2408025	14.50877034	4.791263

We can notice from the table that the PA gain drops with increased input power. The maximum gain as per PA specs is 45 dB but that is at low input power. Going beyond 0.6 amplitude the output starts to reach a constant state. In equation 13 and 14 below, the maximum PA power output (P_{MAX}) at 0.99 will be calculated. In this case the

PA gain (G) will be equal 30 + 4.79 = 34. 79 dB. Input power (P_0) will be equal to power output from 5412 card at 0.99 amplitude in Table II-1.

$$G = 10 \log\left(\frac{P}{P_0}\right) \tag{13}$$

$$P_{MAX} = P_0 * 10^{G/10} = 0.00937 * 10^{34.79/10} = 28.23\ W \tag{14}$$

Knowing that we can get around 28 W from the maximum PA rating which is 30 W. The next step is calculating the maximum current that can run through the excitation coil. $I_{MAX} = (P_{MAX} / R)^{1/2} = (28.23/50)^{1/2} = 0.75$ A. Substituting I_{MAX} in equation 12, 60 windings for N, 4.4 cm for l and 1 cm for r. The DF that can be obtained using the PA and the excitation coil is show below in equation 15 and 17. Equation 16 is the conversion between A/m to $mT\mu_0^{-1}$.

$$H(t) = 1241 * I_{MAX} = 930.75\ A/m \tag{15}$$

$$1\ mT{\mu_0}^{-1} = 4\,\pi * 10^{-3}\ A/m \tag{16}$$

$$H(t) = 930.75 * 4 * \pi * 10^{-3} = 11.69\ mT{\mu_0}^{-1} \tag{17}$$

Having 28 W from the PA and around 12 $mT\mu_0^{-1}$ gives the system enough power for particle excitation. 10 $mT\mu_0^{-1}$ was used for 15 nm particle excitation at an experiment at the University of Washington [13].

II.3.4 Band Pass Filter Implementation

After making sure the PA is up to the task of supplying the required power to the excitation, the next step is to check on the quality of the output signal. In order for the nanoparticles to be excited using a varying magnetic field, the sinusoid produced by the 5412 card and the PA has to be a clean sinusoid, carrying no unwanted harmonics. Using the previous setup in Figure II-4, the shape of the sinusoid at different 5412 card amplitudes can be monitored. Increasing the 5412 card amplitude past 0.5 the sinusoid loses its clean curve shape carrying unwanted harmonics. In Figure II-5, the obtained shape of the excitation signal is shown.

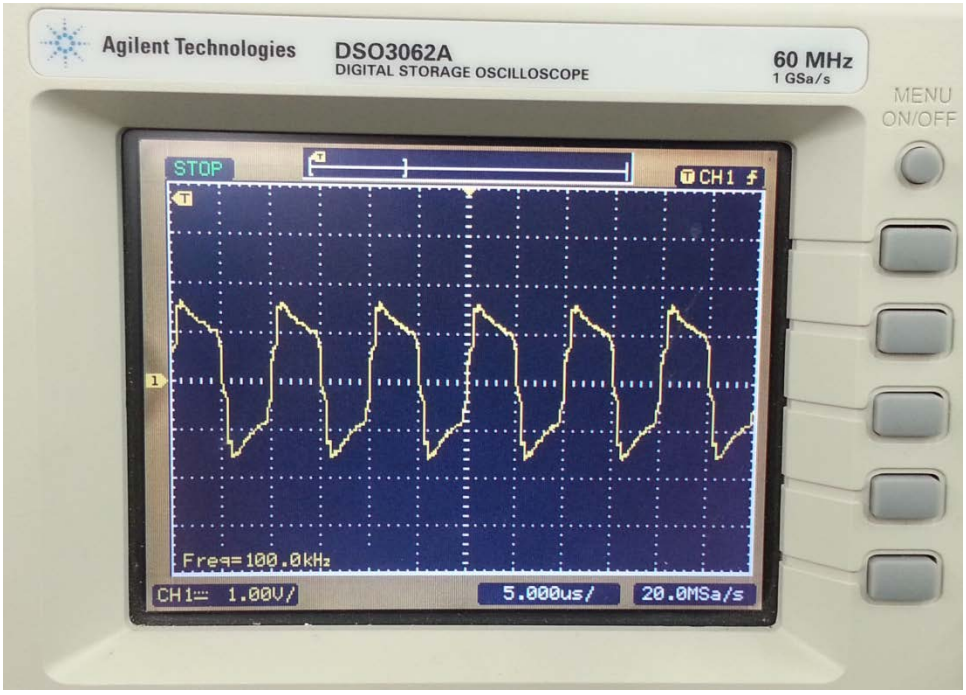

Figure II-5 PA output obtained signal.

The solution to this problem was to implement a lab-built band pass filter centered around f_0 (100 kHz). The chosen filter design is a 2nd order Butterworth Pi topology band pass filter with Q = 10 (Q = center frequency / bandwidth). The circuit design was simulated using LTspice IV below in Figure II-6. The simulation shows a center frequency of 100 kHz and minimum insertion loss. At Phillips Research, researchers are in the process of developing high quality sinusoidal output using pulse-width-modulated and multilevel-inverter based amplifiers. These amplifiers are for straight use for MPI drive fields instead of using filtering [14].

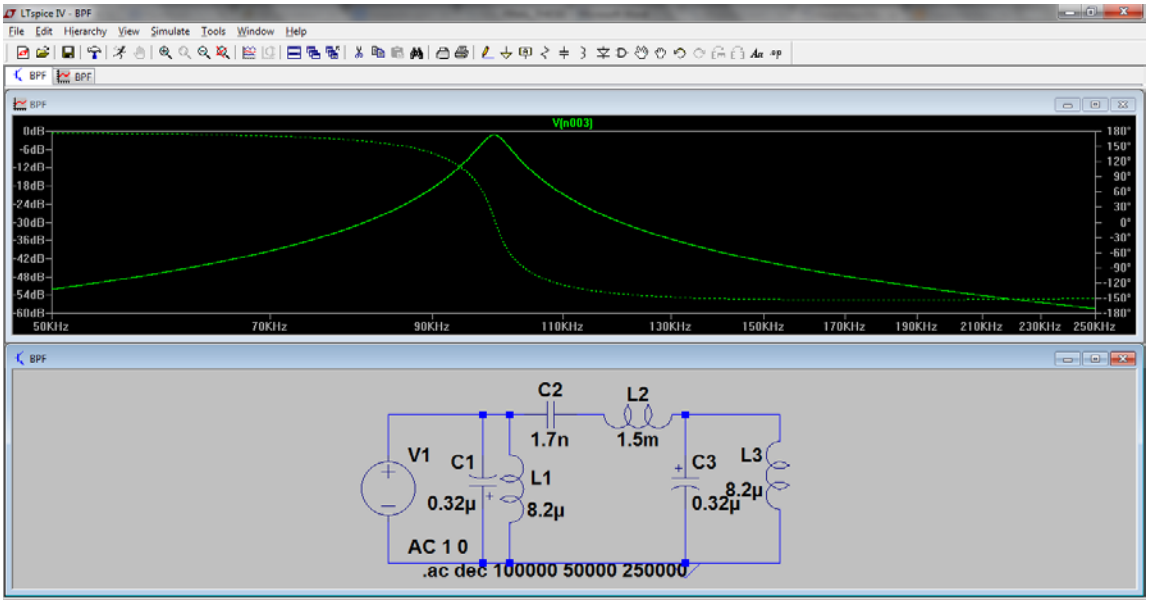

Figure II-6 Band pass filter simulation.

After the components were purchased and the filter was built, we included the filter in the testing setup. We ran the system to check the shape of the output signal. We

ran the system at 0.99 5412 card amplitude to check the effectiveness of the band pass filter at maximum power. In Figure II-7, the obtained shape of the excitation signal is shown. We can notice that the band pass filter signal output is clean and does not consist of unwanted harmonics.

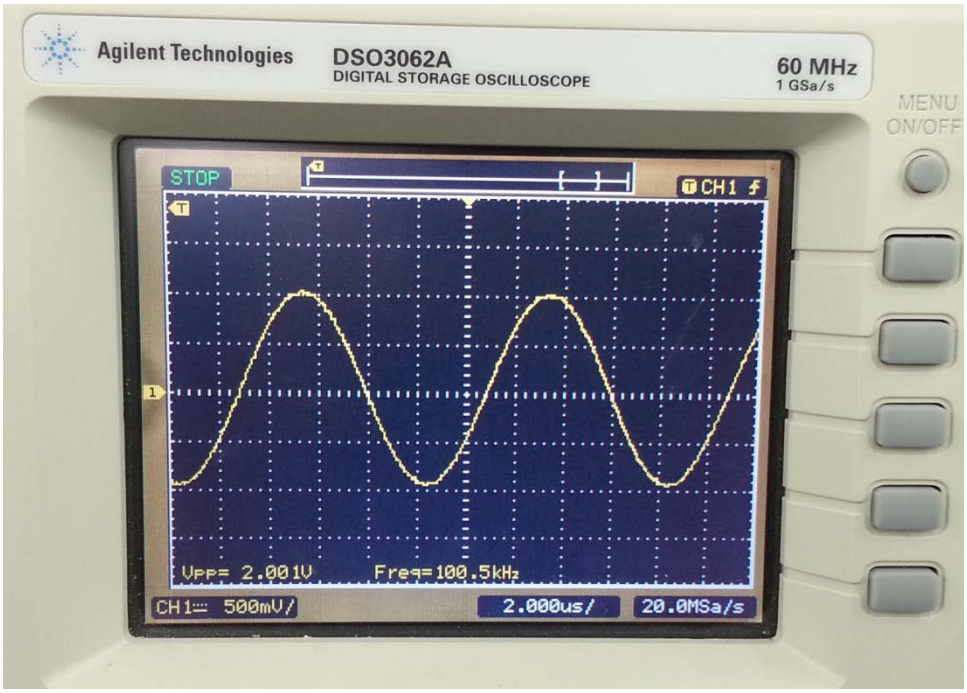

Figure II-7 Band pass filter clean sinusoid signal output.

Although the signal is clean as required, it's noticed that at 0.99 amplitude the signal amplitude after the band pass filter decreased. This is due to the insertion loss of the filter. Insertion of the filter cannot be only known through simulation. An S21 mode test was made using the lab network analyzer. The center frequency was set to 100 kHz and the span to 20 kHz. In Figure II-8, it's shown that at 100 kHz, the band pass filter had a 5.389 dB insertion loss.

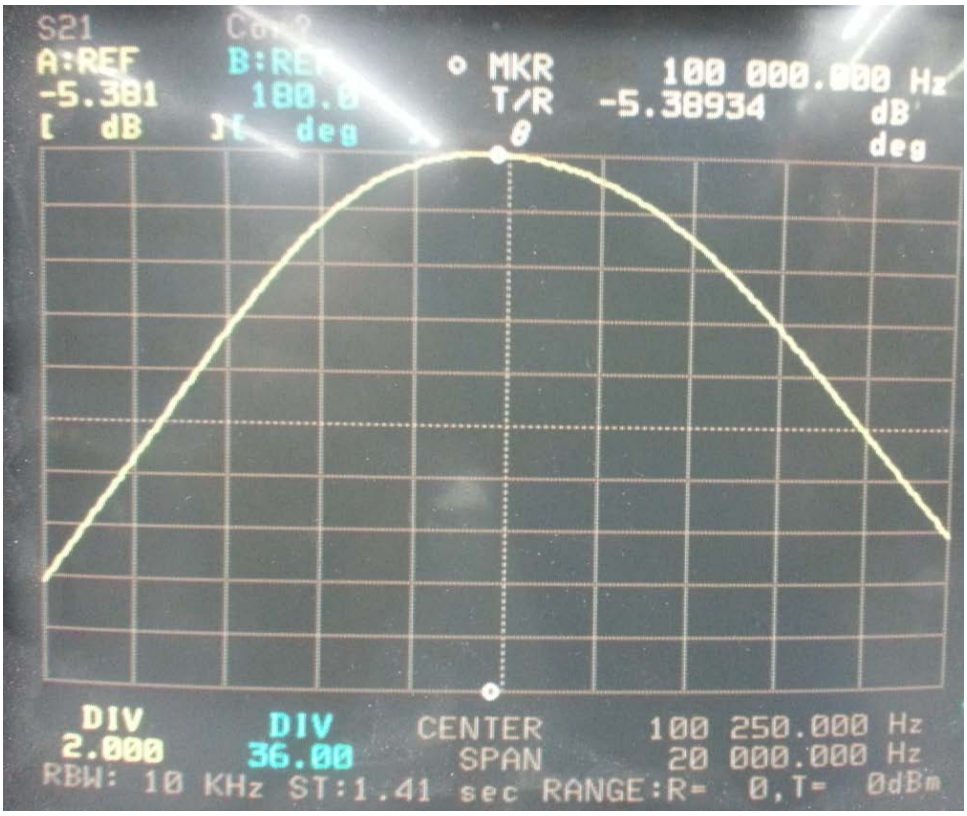

Figure II-8 Demonstration of band pass filter insertion loss using network analyzer.

Moreover a table (Table II-3) was obtained like the tables before of all the amplitude of the sinusoid after the band pass filter was added to the system. We can calculate the filter gain by subtracting the power in dBm from Table II-2 from the power in dBm in Table II-3. The value of the gain is negative due to the fact that there is an insertion loss. The overall gain can be calculated by adding the gain from Table II-2 to the attenuation to the filter gain. After implementing the band pass filter we will have around 10 W at the output. The DF has to be recalculated, $I_{MAX} = (P_{MAX} / R)^{1/2} =$

$(10.01/50)^{1/2}$ = 0.447 A. The DF that can be obtained using the PA, the excitation coil and the band pass filter is show below in equation 18. Around 7 $mT\mu_0^{-1}$ is still an appropriate magnetic field for the nanoparticles to experience most of the dynamic range magnetization change.

Table II-3 Band pass filter power output.

AMP	Vpp(mV)	Power(W)	P (dBm)	Filter Gain	Overall Gain
0.1	800	1.6	2.0412	-4.08918286	41.70053304
0.2	1241	3.8502025	5.854836	-5.58648411	39.8342358
0.3	1481	5.4834025	7.390501	-5.28346967	37.96466704
0.4	1601	6.4080025	8.067227	-5.2228045	36.20150538
0.5	1641	6.7322025	8.281572	-5.35815678	34.51317527
0.6	1681	7.0644025	8.490754	-5.70222635	33.16249741
0.7	1721	7.4046025	8.695017	-5.39009608	32.04483924
0.8	1761	7.7528025	8.894587	-5.61418313	31.09735278
0.9	1801	8.1090025	9.089674	-5.31510326	30.27934464
0.99	2001	10.0100025	10.00434	-4.50442848	30.28683471

$$H(t) = 1241 * I_{MAX} * 4\,\pi * 10^{-3}$$
$$= 1241 * 0.447 * 4\,\pi * 10^{-3}$$
$$= 6.97\, mT{\mu_0}^{-1} \quad (18)$$

II.3.5 LabView Module

The LabView module that was implemented uses certain parameters to be inputted by the user. The user has to set the center frequency in our case 100 kHz, sampling frequency, pulse amplitude (5412 card amplitude), excitation duration, trigger delay, acquisition time, number of averages and band stop filter frequency range. Trigger delay is the parameter that controls when the 5122 card can start acquiring and digitizing the signal from the receive coil. The PA takes around 1 ms to ramp up to the desired power, that's why there is a trigger delay that ensures the acquisition starts after the excitation signal is stabilized.

The nanoparticle signal in MPI is acquired in the same time frame as the excitation signal, so excitation and acquisition durations are comparable, unlike MRI where acquisition starts later and for a longer period to account for longer relaxation times. Averaging is basically, repeating excitation and digitizing *i* times to increase test confidence and reduce signal to noise ratio (SNR) and consistency. The averaged signal and Fourier transform is the total sum of magnitudes at all sampled points divided by the number of averages or iterations. So as mentioned before, the combination of the non-linear response and the drive field could be expressed using a Fourier transform. As a result of the non-linear relationship the particle signal has not only a peak at the fundamental frequency, f_0, but at all higher harmonics. The objective of this module is to be able to show the higher harmonics in a clear manner. However, since acquisition and digitizing are done at the same time, this means that the receiver coil will be picking up the excitation signal. The excitation signal contaminates the nanoparticle signal at f_0,

consequently the fundamental frequency is filtered using the high pass filter mentioned in the hardware outline earlier. As for the last input, the digital band stop filter is considered an extra filtering to the fundamental frequency. The lower and upper boundaries of the digital band stop filter are 50 and 150 kHz respectively.

The LabView module provides its user with a block diagram and a front panel. The block diagram is where the module's building blocks are inserted to perform a certain function. The front panel is the interface the user needs to communicate with the module. In the front panel, below in Figure II-9, the user inserts the required inputs and sees the output data. The front panel is divided into three tabs. The main tab has the inputs mentioned earlier, the 5412 pulse, the signal received by the receiver coil and the Fourier transform of the received signal. The second tab has the averaging function. The way averaging is programed is that a shift register would save the signal, in array form, from every module run and add it to following run. After all the runs are complete, the accumulated signal array is divided by the number of runs. The number of runs is what we call number of averages. The second tab will have the averaged received signal and its Fourier transform. The third tab has the inputs for the digital band stop filter mentioned earlier along with the filtered signal and its Fourier transform.

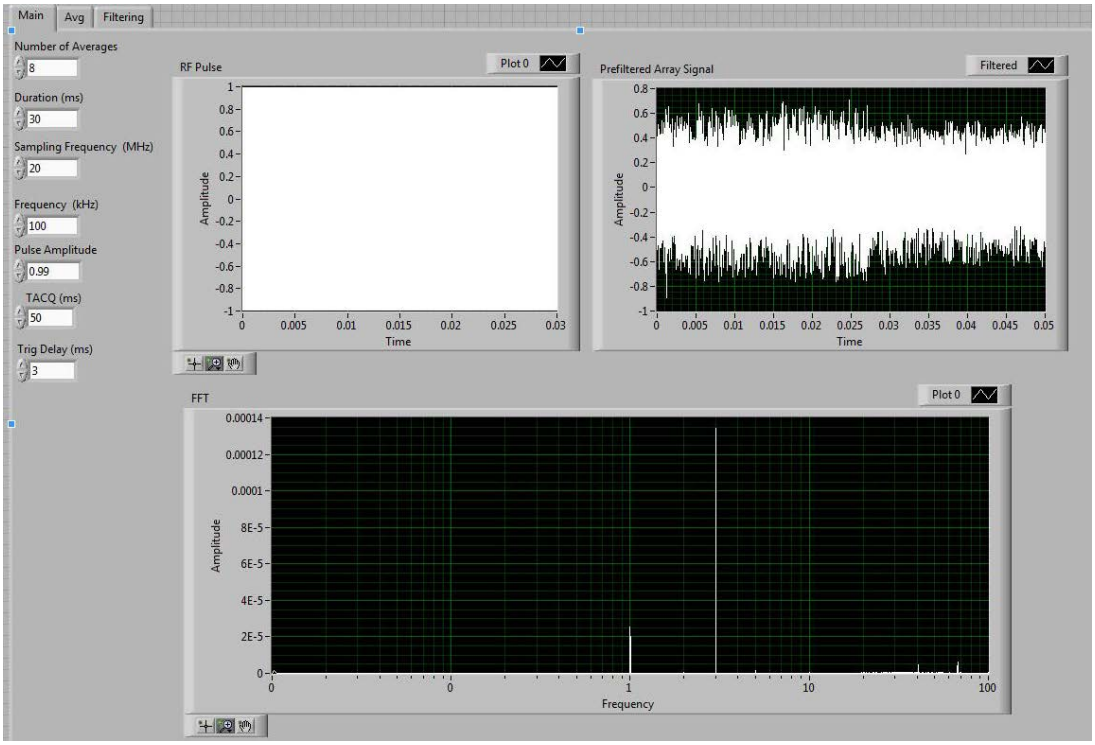

Figure II-9 LabView module main tab.

The last point we need to address is how long the code takes to run. The 5412 and 5122 cards take time to process and digitize. Internal LabView modules such as the module used to run a Fourier transform with every average takes time. Through LabView's tools you can access the module's performance and memory use. One run or average takes around 600 ms. Most of the time is used up in running a Fourier transform to the received signal in every average (400 ms). In Figure II-10, the profile performance and memory window is shown. It shows how much the sub-processes take time and memory space. MPI_v3 is the full LabView module and power spectrum is the internal module that runs Fourier transforms.

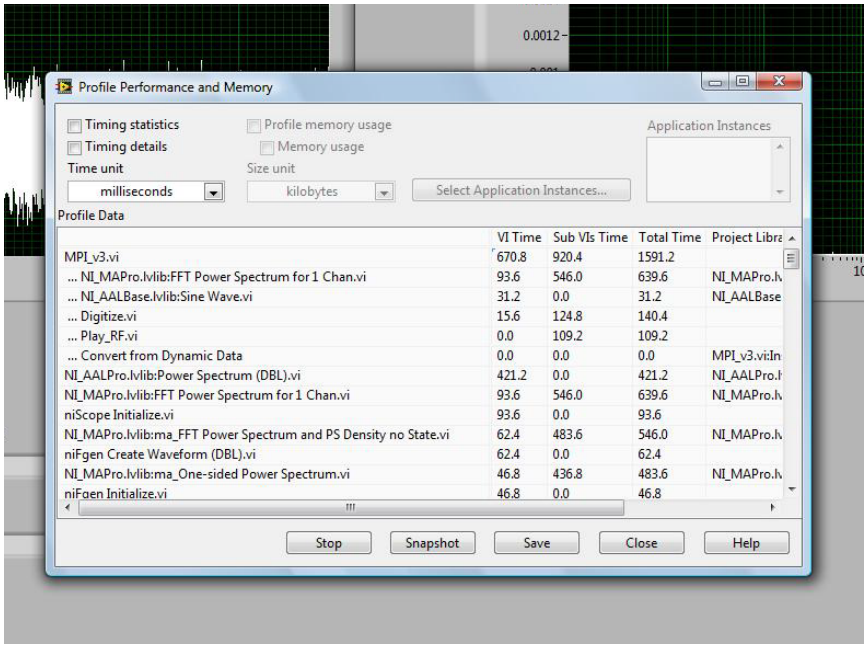

Figure II-10 LabView profile performance and memory window.

CHAPTER III

SYSTEM EXPERIMENTATION

In this chapter, the very first experiments will be made. Most will be of a troubleshooting and debugging nature. Now that the system components are all in sync at 50 ohm, and the DF magnetic field requirement is met, the first batch of tests can be started. The components will all be connected as per the system block diagram in Figure Now that the system components are all in sync at 50 ohm, and the DF magnetic field requirement is met, the first batch of tests can be started. The components will all be connected as per the system block diagram in Figure II-1.

III.1. Receiver Coil Debugging

The reason why the receiver coil is not explained like the other systems components mentioned is chapter II is that its design was not final and did not pass the first tests. The receiver coil we used for the first test is a solenoid placed coaxially in the center of the excitation coil made of 30 windings, 1.1 cm length and a 0.4 cm length. The solenoid is made using 30 AWG laminated copper wire. The receiver coil is unturned to receive a very wide bandwidth. Narrowband MPI, which reduces bandwidth requirement and increases SNR using modulation could also be implemented [15].

The problem that was faced is that the excitation signal picked up by the receiver coil after filtering was too high for the LNA to handle. As a protective measure, the diodes inside the LNA would reflect parts of the signal if its power is too high. This

signal reflection causes unwanted harmonics. As an example below, Figure III-1a, we can see that there are multiple harmonics obtained from the receiver coil from the Fourier transform (left) although the input signal is just a 300 kHz signal. On the right we can see the digitized signal which is a very distorted signal carrying multiple harmonics. Disconnecting the LNA and connecting the receiver coil directly to the 5122 digitizer card we obtain the waveforms in Figure III-1b. On the left we only see one peak at 300 kHz which is the input signal and on the right we see a clean one harmonic signal. Now after we know what the signal coming from the receiver coil looks like, it is concluded that the problem is due to the limitations on the LNA input signal. The straight forward solution is to take the LNA out of the system and digitize directly from the receiver coil. Unfortunately, the solution to this problem is not that simple as the nanoparticle signal is very weak compared to the excitation signal, so without an LNA the nanoparticle signal will not be detected. We can see in Figure III-1 below how the amplitude of the harmonic at 300 kHz decreases from 0.055 to 7*10^-5.

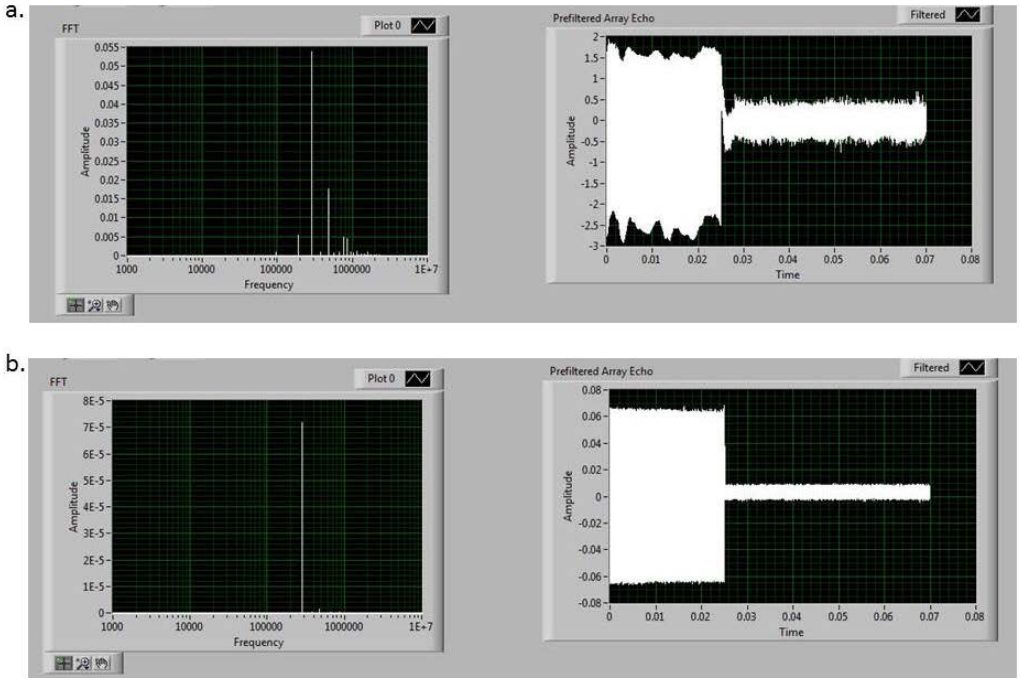

Figure III-1 a. Acquired 300 kHz input signal with LNA. b. Acquired 300 kHz input signal without LNA

III.2. Gradiometer Receive Coil

The solution to our problem was to further eliminate the harmonic at the fundamental frequency. This will result is a lower signal at the LNA input so the LNA input signal limitation does not cause future problems. One way is to use a gradiometer receive coil. This coil is built from 2 coils connected to each other separated by a specific distance. The coils have windings opposite in direction such that the signal induced in both coils cancel each other. The gradiometer will be placed inside the excitation coil, as a result the excitation signal picked up by the gradiometer is nullified [16].

The gradiometer (Figure III-2) is made of the same 30 AWG laminated copper as the previous receiver coil. It's made of 2 solenoids, 0.5 cm and 15 windings each, and 1 cm apart. The coil is then encircled by plastic foam to make sure it fits coaxially in the excitation coil.

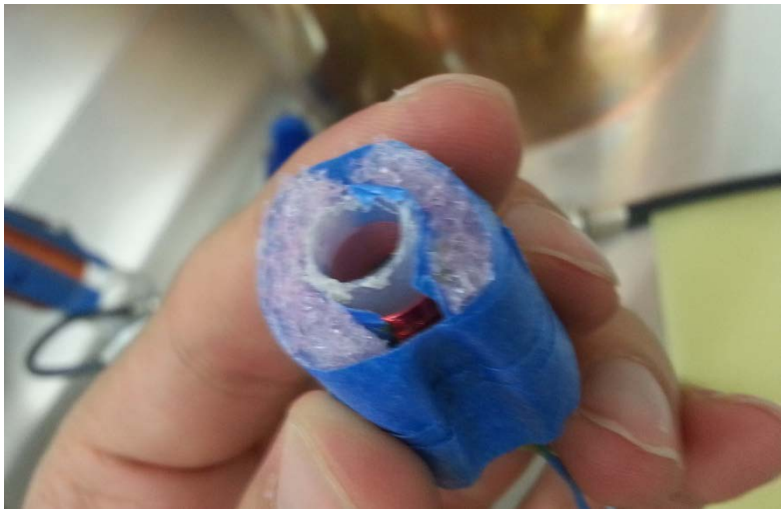

Figure III-2 Gradiometer receive coil.

The next step is to test the gradiometer. Ideally the gradiometer should cancel the harmonic at the fundamental frequency completely. In order for that to happen, both individual coils have to identical and experience the same exact magnetic field inside the excitation coil. The nanoparticles will be placed at the center of only one coil so the nanoparticle signal will not be affected by the cancellation function of the gradiometer. This arrangement can be seen clearly in Figure III-3 below.

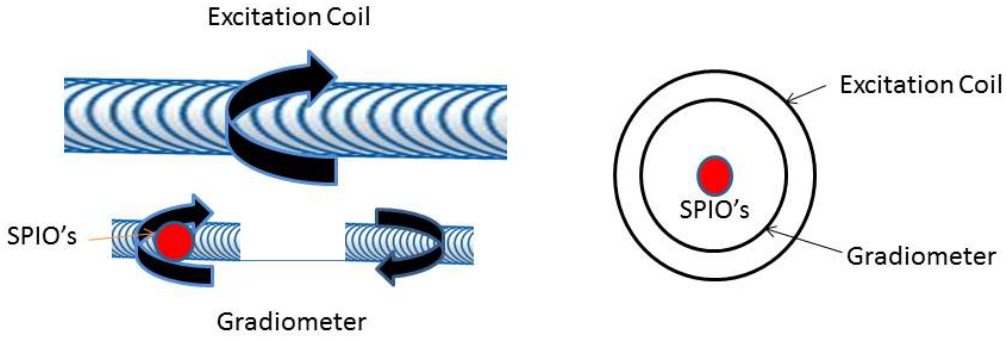

Figure III-3 Excitation coil, Gradiometer and SPIO's assembly.

The gradiometer testing setup will be to test it without an SPIO sample. For this test moving the gradiometer coaxially inside the excitation coil will change the magnetic field experienced by the individual coils. In general, the magnetic field at the center of the excitation coil is where it's most homogenous. So aligning the center of the 1 cm spacing between the individual coils with the center of the excitation coil should make the individual coils experience the same magnetic field, thus maximum fundamental frequency harmonic cancellation. However, this wasn't the case, we obtained maximum cancellation when the left end of the left coil of the gradiometer was almost aligned with the left end of the excitation coil. Since the excitation coil is 4.4 cm long and the entire gradiometer is 2 cm, aligning the center of the 1 cm spacing between the individual coils with the center of the excitation coil leaves us with 11 mm on both ends of the gradiometer. We recorded the amplitude of the fundamental frequency harmonic at different positions (Table III-1). The position of the gradiometer would shift from the center of the excitation coil to the left end of it in 2 mm increments. We used 0.99 amplitude form the 5412 card since we will be requiring maximum power.

Table III-1 Amplitude of the fundamental frequency harmonic at different positions.

Amplitude	Position
4.5E-3	Center
9E-4	2 mm
5E-4	4mm
2E-4	6 mm
2.1E-5	10 mm
9E-5	12 mm

III.3. Excitation and Acquisition Durations

After placing the gradiometer in its optimized position, the next step is find the optimum excitation and acquisition time. Acquisition will be at the same time excitation as mentioned before, only the LabView module starts the acquisition process after a very short trigger delay to allow for the excitation signal to stabilize. Trigger time set for all the experiments is 3 ms. Neel and Brownian relaxations times are in the region of a few ns and a few μs respectively, these short relaxation times are the reason why we excite and acquire at the same time [7]. In most of the experiments performed, the 3rd harmonic will be our focus since it's the strongest and mainly used for nanoparticle signal detection [17].

Using a small plastic test tube, a 0.05 mL sample of OceanNanotech 25 nm SPIO's is inserted in the gradiometer, making sure the particles is in the center of only one of the individual coils. We only want the nanoparticle signal induced in one coil to avoid nanoparticle signal cancellation. We use full power 0.99 amplitude (5412 card

amplitude), 30 ms excitation pulse and 32 averages. First in Figure III-4, we present the amplitude of the 3rd harmonic response with no SPIO sample in the gradiometer so we can recognize the nanoparticle signal when the SPIO sample is used later. The acquisition time for the first test is 30 ms. On the right side we see the Fourier transform of the received signal (left side) when no SPIO sample is used. We notice that the amplitude of the 3rd harmonic is 8.903E-8. The amplitude at the fundamental frequency is always between 2E-5 and 9E-5 depending on the acquisition time used, when acquisition time increases the amplitude of all the harmonic decreases. In Table III-1 when the least fundamental frequency harmonic was acquired, we used 30 ms excitation and 50 ms acquisition times.

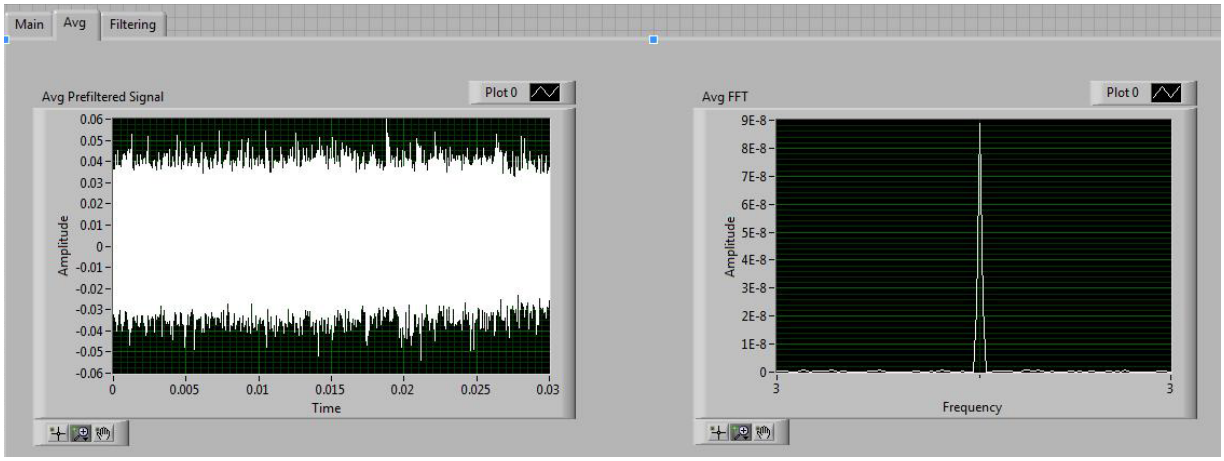

Figure III-4 Amplitude of the 3rd harmonic response with no SPIO sample in the gradiometer at 30 ms excitation and 30 ms acquisition times.

Now we want to check how changing the acquisition time affects the amplitude of the 3rd harmonic when a 0.05 mL of SPIO's is used. In Figure III-5 below, keeping

the excitation duration constant, full power and 32 averages, we see on the right side in the Fourier transform the amplitude of the 3rd harmonic jumps to 0.0103, this jump is almost 5 orders of magnitude confirming the system's detection of the particles. On the left side we also see a higher received signal reaching a peak of 0.2 compared to 0.05 before.

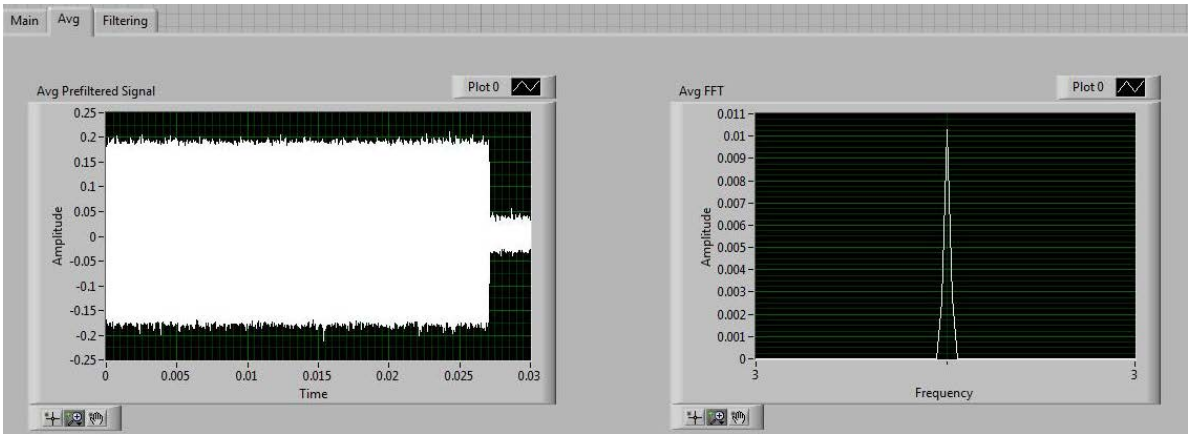

Figure III-5 Amplitude of the 3rd harmonic response with 0.05 ml 25 nm SPIO sample in the gradiometer at 30 ms excitation and 30 ms acquisition times.

In Table III-2 below, the rest of the values of the amplitude of the 3rd harmonic response are recorded for different acquisition times. We notice that increasing the acquisition time cause the amplitude of the 3rd harmonic response to decrease. For the last two measurements though, although acquisition lasted less than excitation, we obtained almost the same exact values for amplitude of 3rd harmonic. In this case, scientists will always prefer less acquisition time because it's more efficient and total image acquisition time decreases, however, comparing using 30 ms to 20 ms acquisition time, in Figure III-6, we noticed that beyond the 9th harmonic, some visible harmonics

decreased in magnitude. Although all the experimentation focuses on the 3rd harmonic, having other visible harmonics beyond the 9th harmonic is beneficial especially in image reconstruction later on. Accordingly, we will be adhering to same excitation same acquisition durations.

Table III-2 Amplitude of the 3rd harmonic response for corresponding acquisition times.

Acquistion Time	**Amplitude of 3rd Harmonic**
30	0.0103
40	0.00661
50	0.00336
60	0.00162
10	0.0098
20	0.00985

a.

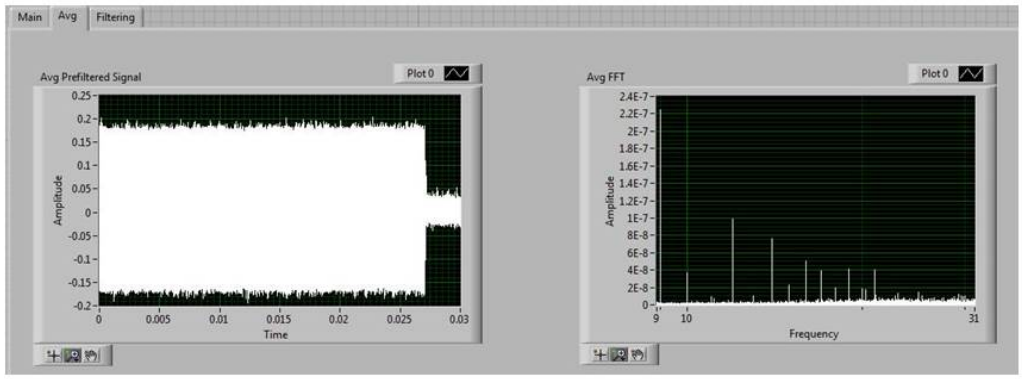

b.

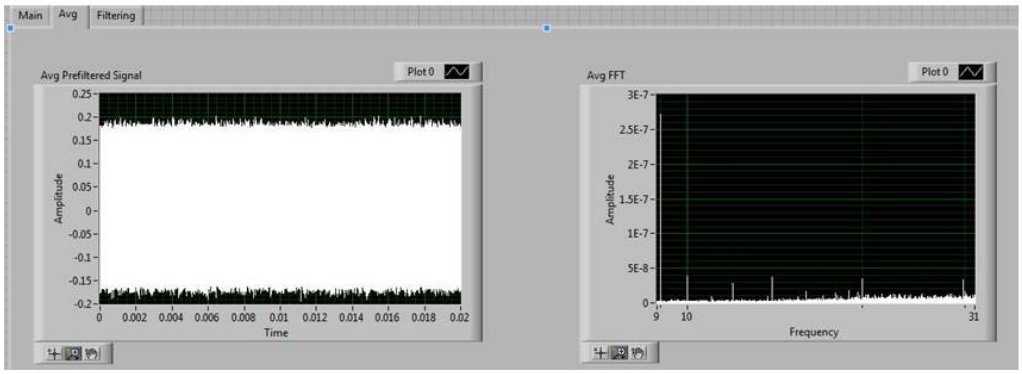

Figure III-6 a. The obtained harmonics at 30 ms acquisition time beyond 9th harmonic. b. The obtained harmonics at 20 ms acquisition time beyond 9th harmonic.

CHAPTER IV

TESTING AND RESULTS

IV.1. Final System

The final system that will be used for the testing and results is shown in Figure IV-1 and Figure IV-2. In Figure IV-1, at the far left we see the NI-133 chassis. The chassis includes the 5412 and 5122 cards. Next is the DC power supply used to power the LNA and the LNA is right in front of it. Next is the PA, with its heat sink below it. Next is the lab-built band pass filter. Next is a cylindrical copper shield that houses both the excitation and gradiometer coils. In Figure IV-2 a, the side view shows the copper shield and the high pass filter. In Figure IV-2 b, the top view shows foam supporting the plexiglass tube which has the excitation coil winded around it. The small copper box is the shielded matching circuit. The gradiometer is placed through the center of the tube. The thick black cable is the cable that provides the excitation coil with power through the PA and the band pass filter. The thin cable is the cable coming from the gradiometer carrying the nanoparticle signal through the high pass filter then to the LNA.

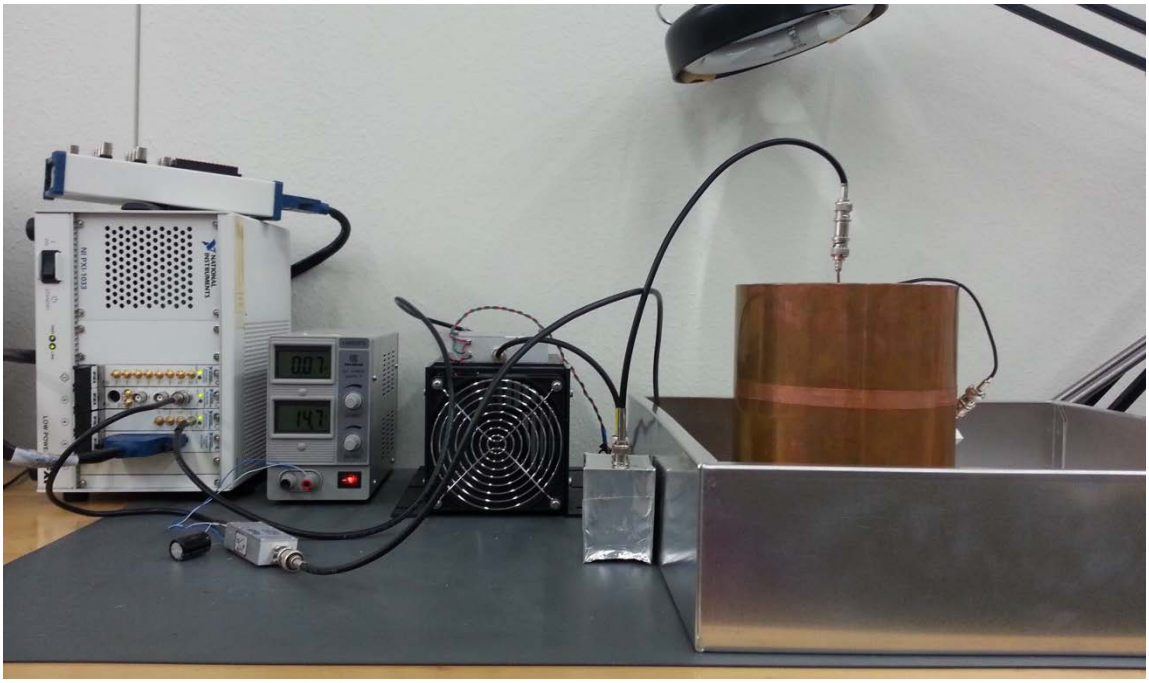

Figure IV-1 Final system appearance showing its separate components.

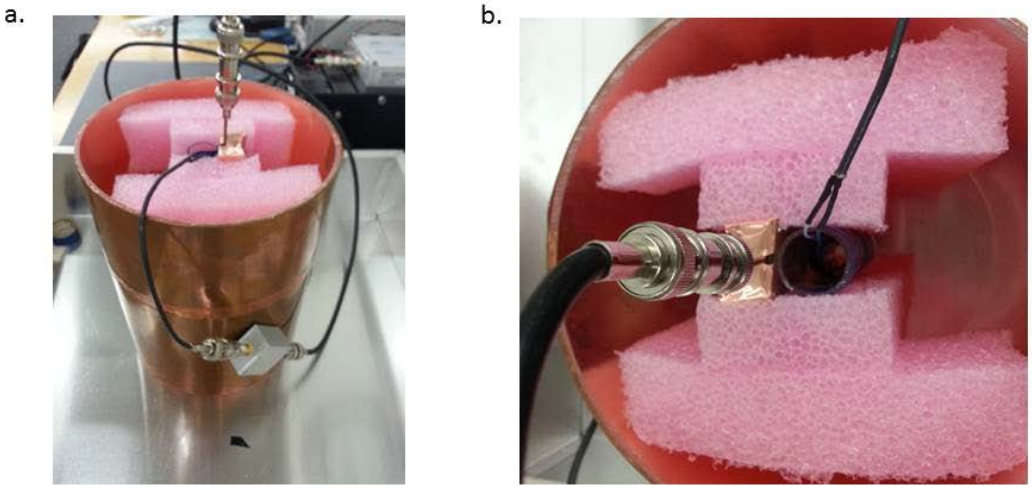

Figure IV-2 a. Excitation and receiver coil setup side view b. Excitation and receiver coil setup top view.

IV.2. Testing Ocean Nanotech 25 nm SPIO's

After all of the components are in place, gradiometer position is optimized, and acquisition and excitation times are determined, it is time for the first time use of the relaxometer. In the following next set of tests we plan to reduce the acquisition time slightly. As we can see Figure III-5, on the left the averaged signal drops in magnitude during the last 3 ms of acquisition. This decrease is due to the 3 ms trigger time. So in order to have exactly same excitation and acquisition times, excitation time will be 28 ms and acquisition time will be 25 ms.

Four tubes of Ocean Tech 25 nm SPIO's was prepared. As mentioned earlier the concentration of iron oxide is 5 mg/mL. The four tubes have volumes of 0.05, 0.1, 0.2 and 0.4 mL. The first step to perform before a test is to run the system with no SPIO sample to check the magnitude of the fundamental frequency and to check if the receiver coil is picking up any unwanted harmonics, which might contaminate the SPIO signal. In Figure IV-3, we see as expected a fundamental frequency amplitude value of 2.97E-5. This value and the absence of visible larger harmonics means the system is ready for further tests.

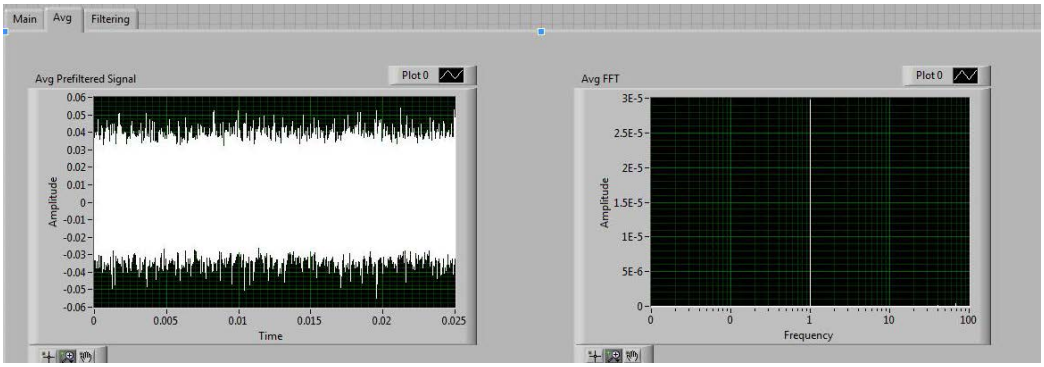

Figure IV-3 Amplitude of fundamental frequency response with no SPIO sample in the gradiometer at 28 ms excitation and 25 ms acquisition times.

Using 0.99 amplitude (5412 card), 28 ms excitation, 25 ms acquisition time and 32 averages, in Figure IV-4 up to Figure IV-7, 0.05 mL up to 0.4 mL of SPIO was inserted in the gradiometer respectively. The amplitude of the 3rd harmonic responses are recorded in Table IV-1 below.

Table IV-1 Amplitude of the 3rd harmonic response for corresponding volumes of 25 nm SPIO's.

Volume (mL)	**Amplitude of 3rd Harmonic**
0.05	0.00971
0.1	0.0315
0.2	0.0499
0.4	0.0563

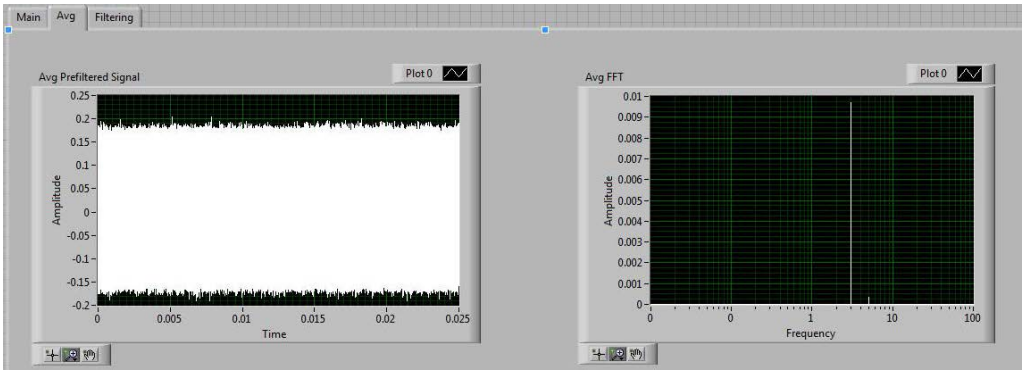

Figure IV-4 Amplitude of 3rd harmonic response with 0.05 mL 25 nm SPIO sample in the gradiometer at 28 ms excitation and 25 ms acquisition times.

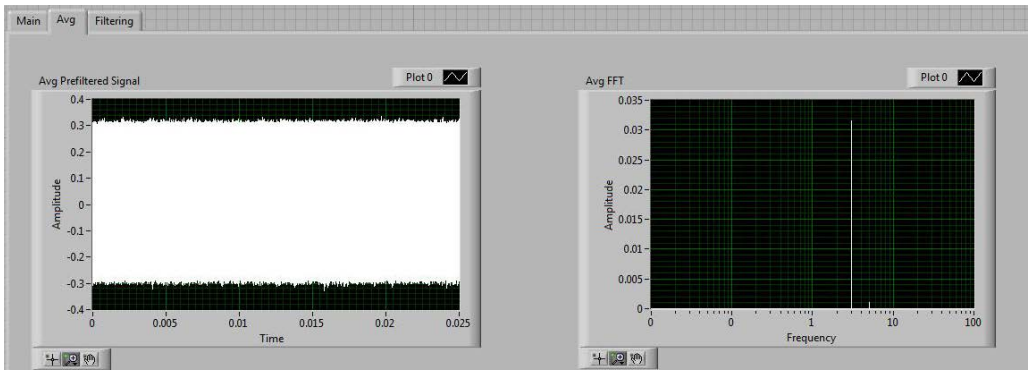

Figure IV-5 Amplitude of 3rd harmonic response with 0.1 mL 25 nm SPIO sample in the gradiometer at 28 ms excitation and 25 ms acquisition times.

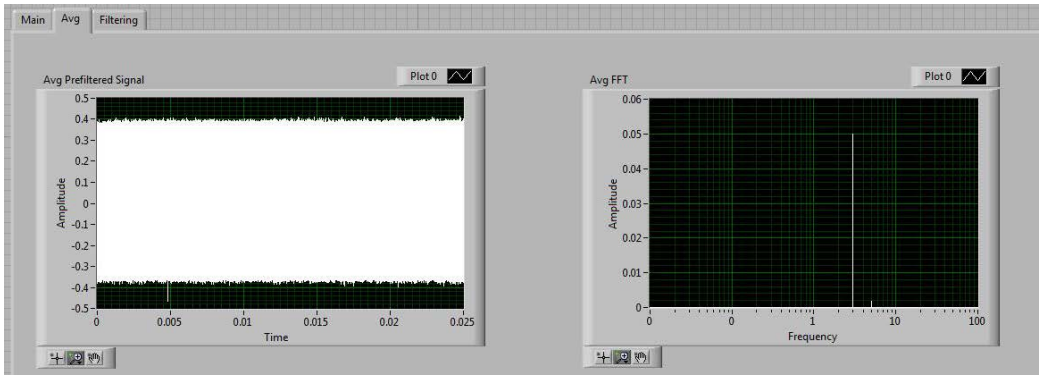

Figure IV-6 Amplitude of 3rd harmonic response with 0.2 mL 25 nm SPIO sample in the gradiometer at 28 ms excitation and 25 ms acquisition times.

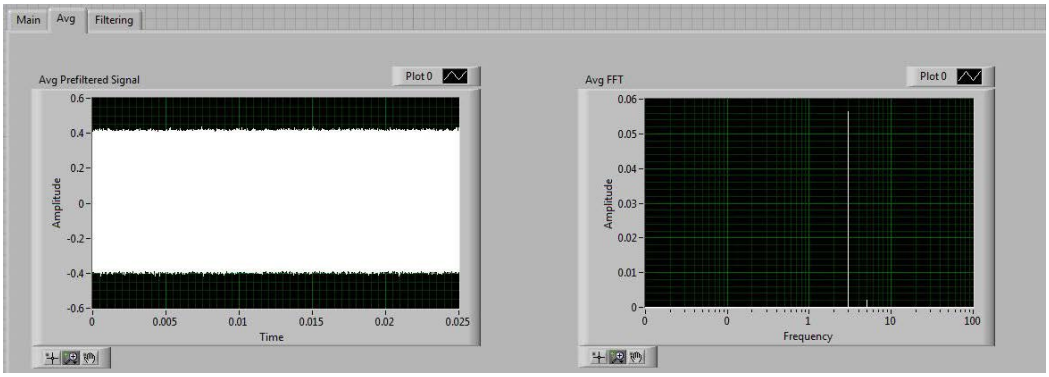

Figure IV-7 Amplitude of 3rd harmonic response with 0.4 mL 25 nm SPIO sample in the gradiometer at 28 ms excitation and 25 ms acquisition times.

We notice that the amplitude of the 3rd harmonic response increases with increasing the volume of the SPIO sample. Since we have a constant concentration this means that the amount of iron oxide increases with increasing volume. Going back to equation 1 in chapter I, we see that the particle magnetization is directly proportional to the concentration or amount of the nanoparticles present, thus we expect the amplitude of the 3rd harmonic to be directly proportional to the volume of the SPIO sample used. In Figure IV-8, we plot the amplitude of the 3rd harmonic response versus the volume of the SPIO sample. The increase in amplitude starts steadily then the increase decreases. The probable reason of the decrease is that when the sample size increases in the plastic tube, the whole sample is not exposed to the same exact excitation field everywhere. As a result parts of the sample do not give off the same received signal. Nonetheless, an increase in the amplitude of the 3rd harmonic response confirms that the relaxometer detects the increase in SPIO concentration.

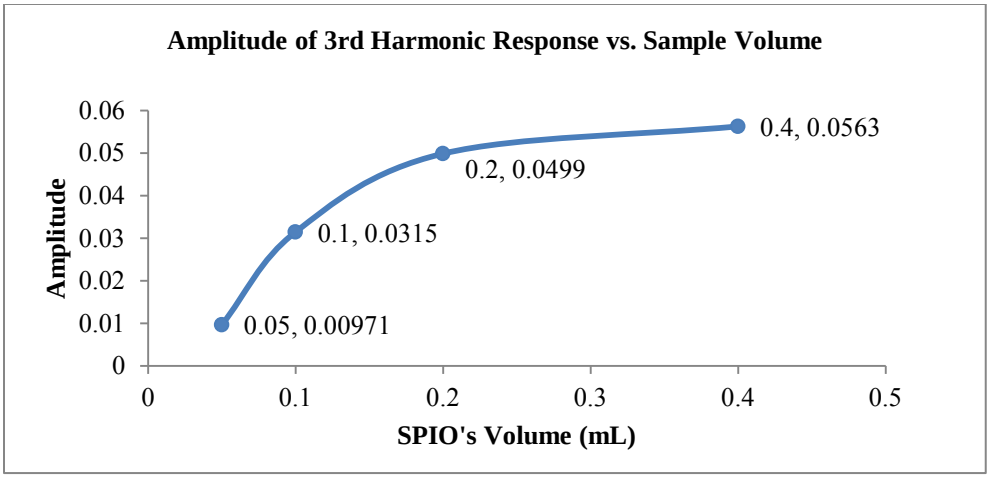

Figure IV-8 Plot of amplitude of 3rd harmonic response vs. sample volume.

Checking the linearity of the relationship between the amplitude of the 3rd harmonic response and the amount of SPIO's, the coefficient of determination method can be used to confirm the relationship. R^2 of a value of 0.7644 means that we have more than 70 percent of the variation can be explained (Figure IV-9).

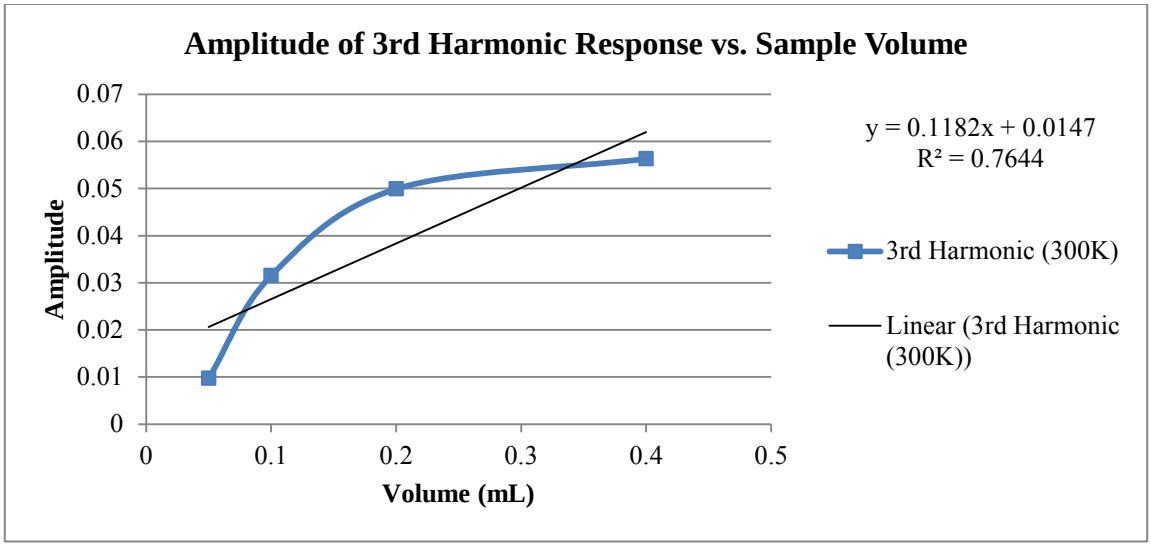

Figure IV-9 Plot of amplitude of 3rd harmonic response vs. sample volume, coefficient of determination method with $R^2 = 0.7644$.

IV.3. Testing Micromod GmbH 250 nm SPIO's

The next test we performed is to use a different diameter SPIO. 250 nm SPIO nanoparticles were purchased from Micromod, GmbH, Germany. The nanoparticle sample has a 25 mg/mL which is 5 times the Ocean Nanotech 25 nm sample. This means we have more SPIO and a larger diameter. Making a quick decision on the amplitude of the 3rd harmonic response we would be expecting a higher response than when using 25 nm. Going back to chapter I, we need to take into consideration type of relaxation and the excitation frequency. Larger particles have a larger hydrodynamical and iron core volume, need lower excitation field magnitude, and have larger relaxation times. But at higher frequencies and higher magnitude magnetic fields Néel motion tends to dominate the efficient relaxation time [6-11].

We conclude in this case that even a larger iron core does not guarantee a larger harmonic response, as the scientist needs to take into account that larger particles have larger relaxation times relax. The next point to consider is if those relaxation times will not degrade the SPIO signal at a given excitation frequency. To support this conclusion, Ferguson at University of Washington, for example states that there is an optimum SPIO diameter for 250 kHz excitation which is 15 nm [13].

In Table IV-2, we can see the amplitude of 3rd harmonic response for 250 nm drop in value, this is due to the fact that the increased relaxation times for those particles affect the speed of their magnetic moment response due to 100 kHz excitation frequency.

Table IV-2 Amplitude of the 3rd harmonic response for corresponding volumes of 250 nm SPIO's at 300K.

Volume (mL)	Amplitude of 3rd Harmonic
0.1	0.000792
0.2	0.0014

Knowing that the purchased 250 nm sample has 5 times the concentration meaning that 0.1 ml has the same amount of iron as 0.5 ml as the 25 nm sample. Still a 0.05 mL sample of produces almost 7 times the 3rd harmonic amplitude when compared to 0.2 ml of the 250 nm which has 20 times the amount of SPIO.

IV.4. Temperature Effect on Ocean Nanotech 25 nm SPIO's

Testing the temperature effect was important since it provides the user with more information regarding the particles relaxation. In equations 6 and 7, we can see that particle temperature is one if the factors that determine Brownian and Néel relaxation times. We notice that reducing the temperature increase both relaxation times increase. At 100 kHz frequency we know that an increase of relaxation times will cause the amplitude of the 3rd harmonic response to drop. We cool the particles from room temperature 300 K to 275 K. We can see that temperature will affect the Néel more than the Brownian relaxation due to the exponential. The amplitude of the 3rd harmonic responses for the cooled SPIO's are recorded in Table IV-3 below.

Table IV-3 Amplitude of the 3rd harmonic response for corresponding volumes of 25 nm SPIO's at 275 K
.

Volume (mL)	**Amplitude of 3rd Harmonic**
0.05	0.00598
0.1	0.0183
0.2	0.0326
0.4	0.0377

We can see that the amplitude almost halves in value. This also tells helps us support our conclusion that Néel relaxation dominates the efficient relaxation due to the significant reduction in 3rd harmonic response amplitude. A small change in the amplitude values suggests that the particles motion is dominated by Brownian motion. Moreover, increasing the temperature will increase the amplitude of the harmonics, but increasing the temperature increases the saturation field required (equation 5) to put the SPIO's in saturation which reduces spatial resolution when it comes to imaging [18]. Imaging will be explained in the next chapter. In Figure IV-10, we see in the plot how the amplitudes reduce in value.

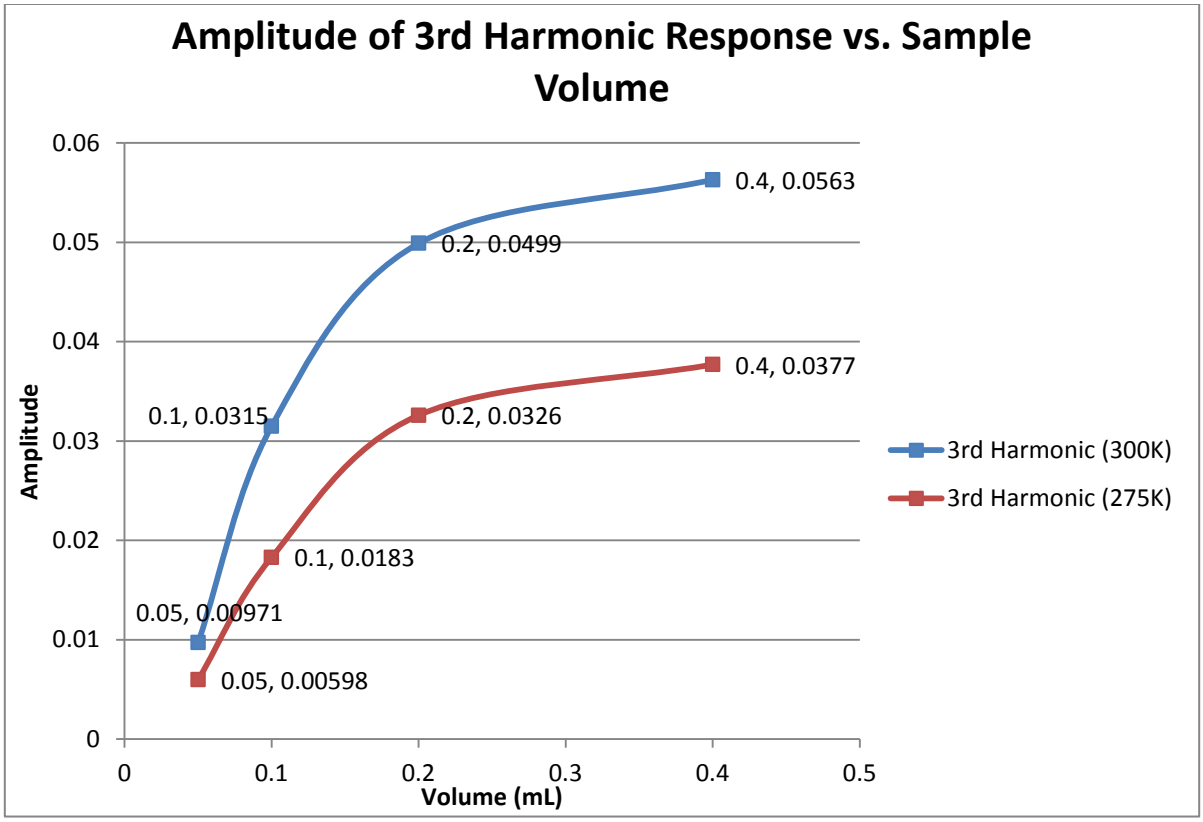

Figure IV-10 Plot of amplitude of 3rd harmonic response vs. sample volume at both 300K and 275K.

We also notice the same increase pattern as the increase is linear at the first part and then the increase slows down. We concluded before that the reason is that the entire sample is not exposed to the same excitation field magnitude everywhere. In the next test, we will be working with a very small amount of SPIO's, starting with one drop of 25 nm SPIO's. The syringe in use allows for accurate 1 drop increases.

IV.5. Re-testing Ocean Nanotech 25 nm SPIO's

Re-testing the 25 nm SPIO's with smaller amounts will help us determine if the 3rd harmonic response is linear vs. the amount of iron present. Moreover, using smaller amounts taking up less space in the tube makes the particles experience similar magnetic fields. In Table IV-4 below, we recorded the amplitude of the 3rd harmonic responses for the drops of SPIO's. We also took a measurement of the amplitude of the 3rd harmonic for 0.05 ml of 25 nm SPIO's. The amplitude of the 3rd harmonic response was 0.01023. This value tells us that 0.05 mL is between 2 and 3 drops volume wise. In Figure IV-11, we see the amplitude of the 3rd harmonic vs. number of drops.

Table IV-4 Amplitude of the 3rd harmonic response for corresponding drops of 25 nm SPIO's.

Number of Drops	Amplitude of 3rd Harmonic Response
1	0.00016198
2	0.006534
3	0.01301
4	0.01826
5	0.024581
7	0.0330613

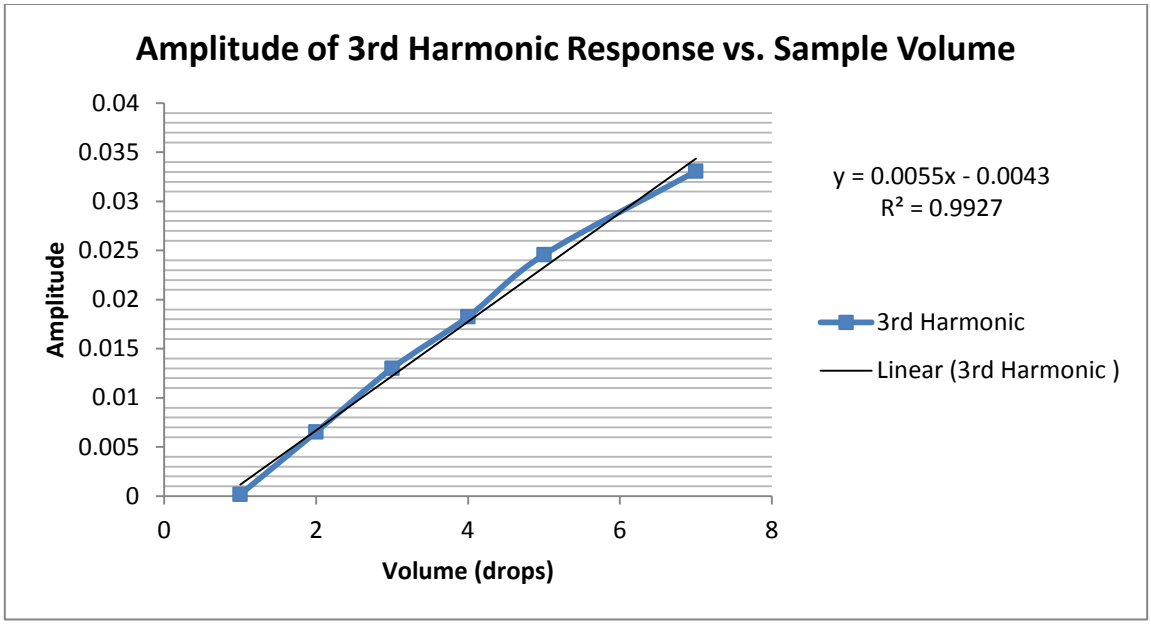

Figure IV-11 Plot of amplitude of 3rd harmonic response vs. sample volume in drops.

Checking the linearity of the relationship between the amplitude of the 3rd harmonic response and the amount of SPIO's, the coefficient of determination method can be used to confirm the relationship. R^2 of a value of 0.9927 shows almost a perfectly linear relationship. Although this is a good conclusion, its sets a limitation of the system as only samples up to around 0.2 mL can be tested. Beyond 0.2 mL the samples will not be exposed to the same magnetic field and the received signal would not be accurate. In Figure IV-12 below, the test tubes with drops of SPIO are shown.

Figure IV-12 Test tubes of drops of SPIO, going from left to right we have 7, 4, 3, 2 and 1 drop.

IV.6. SNR

In our entire previous tests we used 32 averages for all the system runs. From MRI we know that SNR to directly proportional to acquisition time or number averages [19]. Looking at the averaging tab in our LabView tab, on the right we can see the Fourier transform after every run. For SNR, we will change the code slightly. For averaging, we will not be dividing by the number of iterations, this will help us see both the signal and noise amplitudes accumulate with every average. We expect the signal to double as we double the number of averages going from 1 to 128 averages, and the noise to increase but at a slower rate. This statement tells us that the SNR ratio is improving with every average. Moreover, Fast Fourier transform module is used in obtaining amplitudes for the signal and noise, previously power Fourier transform was used in order to have more focus on the 3rd harmonic that was the main interest.

We decided to use 1 drop of SPIO for determining SNR. We decided to use the smallest sample we have in order to be close to the noise floor for accuracy. Noise was calculated by averaging all the sampled points' frequency response amplitudes when no sample is in the relaxometer. The amplitude at the fundamental frequency is not used in the calculation, because this response is due to the PA and not considered system noise. We record the noise sum values for 1 to 128 averages with no sample. The next step is to record the values for the amplitude sum of the 3rd harmonic for 1 drop of 25 nm SPIO's, for 1 to 128 averages.

In Table IV-5 below, we can see that the amplitude sum more or less doubles as expected. Moreover, one drop of SPIO's has a high SNR ratio (sample 3rd harmonic amplitude sum / noise sum value) as can be seen the ratio is around 100 for one average. This high SNR ratio from a very small sample is one of the main advantages of MPI. SQRT (A) is the square root of the averages which is the SNR improvement ratio standard used in MRI. In Figure IV-13, we see the plot the Noise Sum vs. number of averages. The Noise sum shape follows SQRT(A) and does not double like the Amplitude sum as expected. After normalizing the SNR, we plot it alongside the plot of SQRT(A). We can observe that they are identical. The SNR improvement is expected to reach a limit for large acquisition times or large number of averages due to noise domination in the system [20].

Table IV-5 SNR ratio improvement values with averaging.

Averages (A)	**Amplitude Sum of Averages**	**Noise Sum of Averages**	**SNR**	**Normalized SNR**	**SQRT (A)**
1	0.0110697	0.000108364	102.15	1.000	1.000
2	0.0212187	0.000152856	138.81	1.359	1.414
4	0.0439404	0.000216592	202.87	1.986	2.000
8	0.08745	0.000306807	285.03	2.790	2.828
16	0.180196	0.000442556	407.17	3.986	4.000
32	0.361427	0.000643374	561.77	5.499	5.657
64	0.727468	0.000913629	796.24	7.795	8.000
128	1.46018	0.00124109	1176.53	11.517	11.314

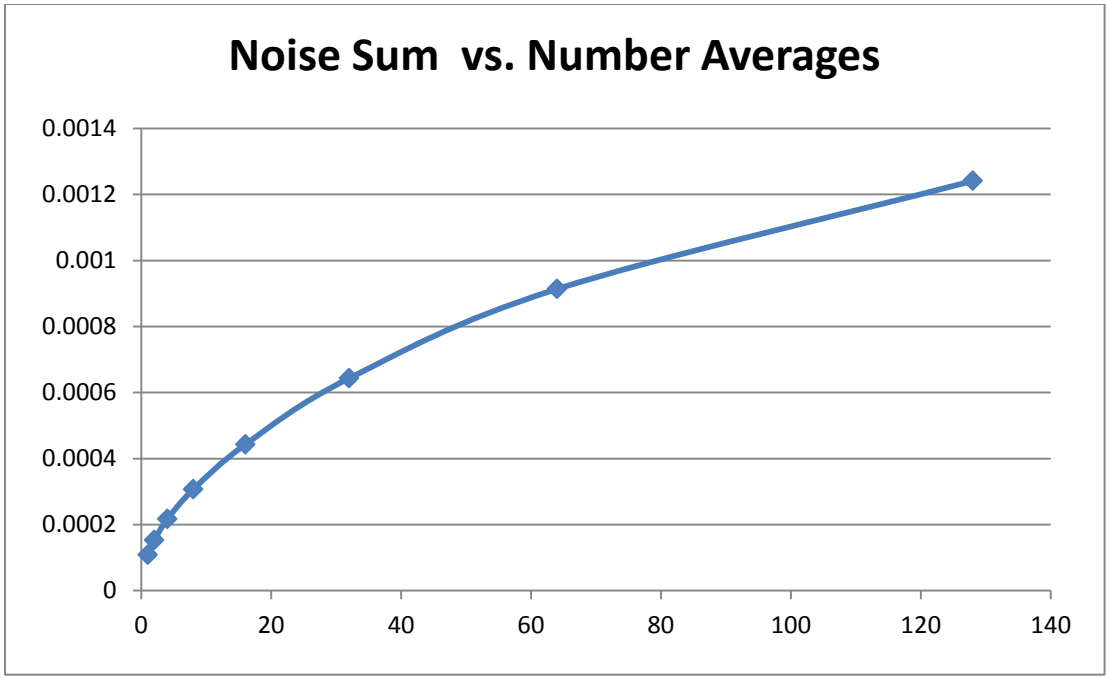

Figure IV-13 Plot of Noise Sum of averages vs. Number of Averages.

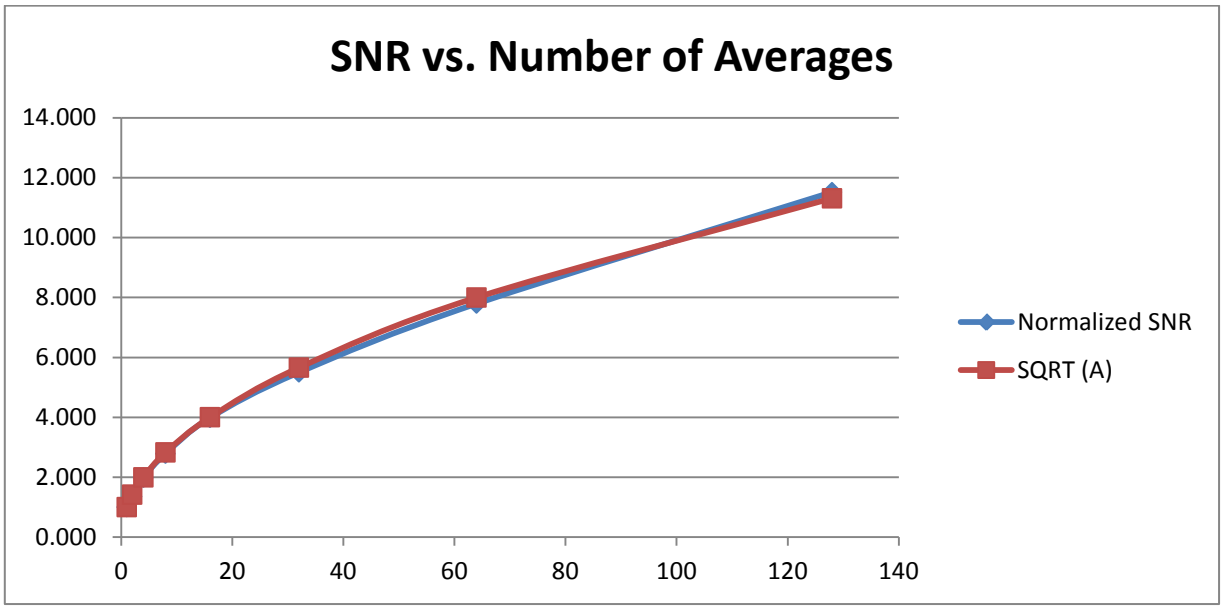

Figure IV-14 Plot of SNR ratio improment vs. number of averages.

CHAPTER V

FUTURE WORK, SAFETY CONCERNS AND APPLICATIONS

V.1. Improved Relaxometer

An improved relaxometer would be able to measure the magnetic particle point spread function (PSF) which is the derivative of the Langevin equation representing the particle's magnetization. The potential resolution of an imaging system is the full width at half maximum (FWHM) of the PSF. Resolution will be discussed in the next section. The other improvement is to have an excitation frequency sweep to be able to test the nanoparticles at different frequency and how the relaxation affects it. [4, 6, 21]

V.2. Imaging

The continuation to this project is to be able to acquire images. We will be starting with the basic concepts first. Going back to the introduction chapter, we need to recall how the magnetic nanoparticles experience saturation. Magnetic nanoparticles will experience saturation when a large constant magnetic field is applied keeping the nanoparticle's magnetic moment at a maximum or a minimum depending on the direction of the field. Moreover, if a smaller varying magnetic field (DF) is applied to the same nanoparticles, a very small received signal will be obtained due to initial nanoparticle moment saturation because of the stronger constant field.

The main objective in imaging is to localize the received signal. If we can receive a signal from multiple points in a sample, using several image reconstruction methods,

this image can be reconstructed. Gleich and Weizenecker suggested the use of a large magnitude gradient [1]. The gradient's magnetic field increases from a large negative value to a large positive value, leaving a point at its center experiencing zero magnetic field. This point is called the field free point (FFP). In this case, the FFP will only be the point responding to a DF. So the general setup they proposed was a set of Helmoltz coils of opposing currents creating the gradient also called a selection field. Within the Helmoltz coils we have the DF coils. Moving the sample within the setup and acquiring the received signal at different points such that we cover the entire sample of field of view (FOV), we can reconstruct an image. The saturation field gradient ranges from around 2 T/m to around 7 T/m [1, 22, 23]. Increasing the gradient increases the spatial resolution of the system, due to the decreased size of sample experiencing zero magnetic field when the same SPIO's are used. For different particles the spatial resolution of the system is calculated by dividing the FWHM / Gradient field. For example, SPIO's with FWHM = 7 mT in a Gradient field of 5 T/m will give a resolution of 7/5 = 1.4 mm. Another method that was used was using a similar approach called a field free line (FLL). For further clarification, to obtain 3D images using a FFP you need three DF coils, but using a FLL you need only two DF coils. FFL showed better sensitivity than FFP imaging when the same concentration of nanoparticles was used. Researchers at Phillips and Berkeley too implemented both FFP and FFL MPI scanners [22-24].

The most published method is using a system matrix that made of the Fourier components of the received nanoparticle signal at every FFP in the FOV. Regularization and matrix inversion methods such as singular value decomposition are used in image

reconstruction. This inversion can be complex due to the large size of the system matrix. [1, 20, 25-28] The second method is a narrowband technique, which uses a modified Wiener deconvolution to reconstruct harmonic images into composite images [15]. The third method is called the X-space reconstruction developed at Berkeley. X-space is considered more efficient than matrix reconstructions. Specifically, X-space MPI is experimentally demonstrated Linear Shift-Invariant images, it consists only division by a scalar to reconstruct each point in the FOV, making real-time image reconstruction possible. No significant noise gain of deconvolution is added since, X-space MPI does not deconvolve the nanoparticle signal to improve resolution [18, 22, 29].

V.3. Safety Concerns

The first concern is regarding the heating accompanied with the magnetic field. The Specific Absorption Rate (SAR) is represented by the heat power of the nanoparticles. For general imaging using MPI, excitation frequencies should not exceed 20kHz for body imaging and 50kHz for brain imaging [18]. Below 50 kHz SAR is within limits and magnetostimulation becomes the main concern.

Regarding magnetostimulation, which is the stimulating of the nerves which causes a slight feeling of discomfort, other studies show that increasing the frequency up to 50 kHz from 25 kHz shows only 6% increase in magnetostimulation thresholds depending on excitation duration. This study also showed that magnetostimulation thresholds where at a minimum when excitation durations were longer than 25 ms [30]. Frequencies around 100 kHz and higher which is the same frequency used in the

relaxometer built in this project can be used for heating therapy called Hyperthermia. Hyperthermia involves heating certain places with tumor to temperatures up to 55ºC to kill cancer cells. However, SPIO's have to be targeted to tumor areas accurately to avoid killing healthy cells [31, 32]. Moreover, further studies on magnetostimulation have to be performed at frequencies above 100 kHz.

V.4. Applications

V.4.1 Angiography

MPI has not been used commercially for human testing yet, but its first main use will be for angiography for patients with chronic kidney disease (CKD). In the USA, 25% of patients who undertake angiography and 47% of patients over the age of 70 suffer from CKD [33-35]. Patients with CKD have no safe angiography method at this time since both Iodine (used for CT scan) and Gadolinium (used for MRI) are processed by the kidneys. SPIO contrast agent is processed by the liver instead and has shown encouraging results with CKD patients [36-38]. Furthermore, SPIO contrast agent Ferumoxytol (AMAG Pharmaceuticals, Lexington, MA) has been approved by the Food and Drug Administration to treat iron deficiency anemia for CKD patients via intravenous injection [39].

V.4.2 Stem Cell Tracking

This method presents a lot of advantages as cells now can be magnetically tagged. In other words the SPIO's would be tagged to the stem cells via chemical process. MPI has very high sensitivity and can track the magnetic tagging. The main

advantage is that MPI is not affected by tissue attenuation and tests show they can detect 5000 cells. Thus, MPI has the potential to be a quantitative, high sensitivity method of cell tracking *in vivo* [40].

CHAPTER VI

CONCLUSION

This thesis introduces researches and engineers in the imaging field to a new imaging modality that has shown encouraging advantages and applications. MPI is considered a safer imaging alternative and promises high spatial resolution and it is not affected by tissue attenuation. The investigation starts with the physical phenomena and SPIO's response to external magnetic fields and types of SPIO relaxation. Next, the objective of a relaxometer, that helps give us an idea about different particle relaxation trends depending on diameter, excitation frequency and other factors in order to choose the best SPIO's for later imaging.

MPI hardware was presented starting with signal generation and amplification, SPIO excitation, receiving SPIO signal. System requirements and limitations, and how the hardware and the software is connected, was also discussed. Two types of SPIO's of diameters 25 nm and 250 nm were tested. Tests included measuring and comparing amplitudes of 3rd harmonic responses of both types. Relaxation of both types at 100 kHz excitation was discussed. The effect of particle temperature on relaxation was tested for the 25 nm SPIO's. The linearity of the relationship between the amplitude of the 3rd harmonic response and the amount of SPIO's was also verified. SNR ratio improvement with the increasing number of averages was also analyzed.

Suggestions for future work include adding features that can improve the relaxometer such as measuring SPIO's PSF and implementing a frequency sweep

function. As mentioned before the continuation to this project is imaging, imaging aspects including gradient and generating a FFP or a FFL was discussed. Leading safety concerns associated with MPI are SAR limits and magnetostimulation. MPI adheres to human SAR limits with excitation frequencies up to 50 kHz. Magnetostimulation thresholds were at a minimum when excitation durations were longer than 25 ms. Future human MPI application that can be implemented are angiography for patients with CKD and stem cell tracking *in vivo*.

REFERENCES

[1] B. Gleich and J. Weizenecker, "Tomographic imaging using the nonlinear response of magnetic particles," *Nature,* vol. 435, pp. 1214-1217, 2005.

[2] C. Ronco, F. Stacul, and P. A. McCullough, "Subclinical acute kidney injury (AKI) due to iodine-based contrast media," *European Radiology,* vol. 23, pp. 319-323, 2013.

[3] J. Weizenecker, B. Gleich, J. Rahmer, H. Dahnke, and J. Borgert, "Three-dimensional real-time in vivo magnetic particle imaging," *Physics in Medicine and Biology,* vol. 54, p. L1, 2009.

[4] P. Goodwill, A. Tamrazian, L. Croft, C. Lu, E. Johnson, R. Pidaparthi*, et al.*, "Ferrohydrodynamic relaxometry for magnetic particle imaging," *Applied Physics Letters,* vol. 98, pp. 262502-262502-3, 2011.

[5] K. Lüdtke-Buzug, S. Biederer, M. Erbe, T. Knopp, T. F. Sattel, and T. M. Buzug, "Superparamagnetic iron oxide nanoparticles for magnetic particle imaging," in *Magnetic Nanoparticles: Particle Science, Imaging Technology, and Clinical Applications: Proceedings of the First International Workshop on Magnetic Particle Imaging*, 2010, p. 44.

[6] T. Knopp, T. M. Buzug, "How Magnetic Particle Imaging Works," in *Magnetic Particle Imaging: An Introduction to Imaging Principles and Scanning Instrumentation*, ed: Springer, 2012.

[7] A. P. Astalan, F. Ahrentorp, C. Johansson, K. Larsson, and A. Krozer, "Biomolecular reactions studied using changes in Brownian rotation dynamics of magnetic particles," *Biosensors and Bioelectronics,* vol. 19, pp. 945-951, 2004.

[8] R. J. Deissler, M. A. Martens, Y. Wu, and R. Brown, "Brownian and Néel relaxation times in magnetic particle imaging " *IEEE Xplore,* 2013.

[9] P. Fannin and S. Charles, "The study of a ferrofluid exhibiting both Brownian and Neel relaxation," *Journal of Physics D: Applied Physics,* vol. 22, p. 187, 1989.

[10] T. Wawrzik, C. Kuhlmann, H. Remmer, N. Gehrke, A. Briel, M. Schilling*, et al.*, "Effect of Brownian relaxation in frequency-dependent magnetic particle spectroscopy measurements," *IEEE Xplore,* 2013.

[11] S. Biederer, T. Knopp, T. Sattel, K. Lüdtke-Buzug, B. Gleich, J. Weizenecker, *et al.*, "Magnetization response spectroscopy of superparamagnetic nanoparticles for magnetic particle imaging," *Journal of Physics. D, Applied Physics,* vol. 42, 2009.

[12] I. Schmale, B. Gleich, J. Kanzenbach, J. Rahmer, J. Schmidt, J. Weizenecker, *et al.*, "An introduction to the hardware of magnetic particle imaging," in *World Congress on Medical Physics and Biomedical Engineering, September 7-12, 2009, Munich, Germany*, 2009, pp. 450-453.

[13] R. M. Ferguson, A. P. Khandhar, K. R. Minard, and K. M. Krishnan, "Size-optimized magnetite nanoparticles for magnetic particle imaging," *Magnetic Nanoparticles: Particle Science, Imaging Technology, and Clinical Application, edited by T. Buzug, J. Borgert, T. Knopp, S. Biederer, TF Sattel, M. Erbe, K. Lüdtke-Buzug,* Singapore: World Scientific Publishing Co, 2010, pp. 53-59.

[14] C. Loef, P. Luerkens, and O. Woywode, "Concept for a Digital Amplifier with High Quality Sinusoidal Output Voltage for MPI Drive Field Coils," in *Magnetic Nanoparticles: Particle Science, Imaging Technology, and Clinical Applications: Proceedings of the First International Workshop on Magnetic Particle Imaging*, 2010, p. 135.

[15] P. W. Goodwill, G. C. Scott, P. P. Stang, and S. M. Conolly, "Narrowband magnetic particle imaging," *Medical Imaging, IEEE Transactions on,* vol. 28, pp. 1231-1237, 2009.

[16] M. Graeser, T. Knopp, M. Grüttner, T. F. Sattel, and T. M. Buzug, "Analog receive signal processing for magnetic particle imaging," *Medical Physics,* vol. 40, p. 042303, 2013.

[17] R. M. Ferguson, K. R. Minard, and K. M. Krishnan, "Optimization of nanoparticle core size for magnetic particle imaging," *Journal of Magnetism and Magnetic Materials,* vol. 321, pp. 1548-1551, 2009.

[18] P. W. Goodwill and S. M. Conolly, "The x-space formulation of the magnetic particle imaging process: 1-D signal, resolution, bandwidth, SNR, SAR, and magnetostimulation," *Medical Imaging, IEEE Transactions on,* vol. 29, pp. 1851-1859, 2010.

[19] A. Macovski, "Noise in MRI," *Magnetic Resonance in Medicine,* vol. 36, pp. 494-497, 1996.

[20] B. Gleich, J. Weizenecker, and J. Borgert, "Experimental results on fast 2D-encoded magnetic particle imaging," *Physics in Medicine and Biology,* vol. 53, p. N81, 2008.

[21] L. R. Croft, P. Goodwill, M. Ferguson, K. Krishnan, and S. Conolly, "Relaxation in X-Space Magnetic Particle Imaging," in *Magnetic Particle Imaging*, Ed. Berlin: Springer, 2012, pp. 149-153.

[22] P. W. Goodwill, K. Lu, B. Zheng, and S. M. Conolly, "An x-space magnetic particle imaging scanner," *Review of Scientific Instruments,* vol. 83, pp. 033708-033708-9, 2012.

[23] J. Weizenecker, B. Gleich, and J. Borgert, "Magnetic particle imaging using a field free line," *Journal of Physics D: Applied Physics,* vol. 41, p. 105009, 2008.

[24] J. Konkle, P. Goodwill, and S. Conolly, "Development of a field free line magnet for projection MPI," in *SPIE Medical Imaging*, 2011, pp. 79650X-79650X-7.

[25] T. Knopp, J. Rahmer, T. Sattel, S. Biederer, J. Weizenecker, B. Gleich*, et al.*, "Weighted iterative reconstruction for magnetic particle imaging," *Physics in Medicine and Biology,* vol. 55, p. 1577, 2010.

[26] T. Knopp, S. Biederer, T. Sattel, J. Weizenecker, B. Gleich, J. Borgert*, et al.*, "Trajectory analysis for magnetic particle imaging," *Physics in Medicine and Biology,* vol. 54, p. 385, 2009.

[27] T. Knopp, S. Biederer, T. F. Sattel, J. Rahmer, J. Weizenecker, B. Gleich*, et al.*, "2D model-based reconstruction for magnetic particle imaging," *Medical Physics,* vol. 37, p. 485, 2010.

[28] J. Weizenecker, J. Borgert, and B. Gleich, "A simulation study on the resolution and sensitivity of magnetic particle imaging," *Physics in Medicine and Biology,* vol. 52, pp. 6363-6374, 2007.

[29] P. W. Goodwill and S. M. Conolly, "Multidimensional x-space magnetic particle imaging," *Medical Imaging, IEEE Transactions on,* vol. 30, pp. 1581-1590, 2011.

[30] E. U. Saritas, P. W. Goodwill, D. Chang, and S. M. Conolly, "Effects of Frequency and Pulse Duration on Magnetostimulation Limits for MPI." *IEEE Xplore,* 2013.

[31] C. C. Berry and A. S. Curtis, "Functionalisation of magnetic nanoparticles for applications in biomedicine," *Journal of Physics D: Applied Physics,* vol. 36, p. R198, 2003.

[32] M. Babincova, P. Sourivong, D. Leszczynska, and P. Babinec, "Blood-specific whole-body electromagnetic hyperthermia," *Medical Hypotheses,* vol. 55, pp. 459-460, 2000.

[33] J. H. Ix, N. Mercado, M. G. Shlipak, P. A. Lemos, E. Boersma, W. Lindeboom*, et al.*, "Association of chronic kidney disease with clinical outcomes after coronary revascularization: the Arterial Revascularization Therapies Study (ARTS)," *American Heart Journal,* vol. 149, pp. 512-519, 2005.

[34] D. N. Reddan, L. A. Szczech, R. H. Tuttle, L. K. Shaw, R. H. Jones, S. J. Schwab*, et al.*, "Chronic kidney disease, mortality, and treatment strategies among patients with clinically significant coronary artery disease," *Journal of the American Society of Nephrology,* vol. 14, pp. 2373-2380, 2003.

[35] J. Coresh, E. Selvin, L. A. Stevens, J. Manzi, J. W. Kusek, P. Eggers*, et al.*, "Prevalence of chronic kidney disease in the United States," *JAMA: the journal of the American Medical Association,* vol. 298, pp. 2038-2047, 2007.

[36] J. Ferrucci and D. Stark, "Iron oxide-enhanced MR imaging of the liver and spleen: review of the first 5 years," *AJR. American Journal of Roentgenology,* vol. 155, pp. 943-950, 1990.

[37] R. a. Weissleder, D. Stark, B. Engelstad, B. Bacon, C. Compton, D. White*, et al.*, "Superparamagnetic iron oxide: pharmacokinetics and toxicity," *American Journal of Roentgenology,* vol. 152, pp. 167-173, 1989.

[38] E. A. Neuwelt, B. E. Hamilton, C. G. Varallyay, W. R. Rooney, R. D. Edelman, P. M. Jacobs*, et al.*, "Ultrasmall superparamagnetic iron oxides (USPIOs): a future alternative magnetic resonance (MR) contrast agent for patients at risk for nephrogenic systemic fibrosis (NSF) &quest," *Kidney International,* vol. 75, pp. 465-474, 2008.

[39] M. Lu, M. H. Cohen, D. Rieves, and R. Pazdur, "FDA report: Ferumoxytol for intravenous iron therapy in adult patients with chronic kidney disease," *American Journal of Hematology,* vol. 85, pp. 315-319, 2010.

[40] B. Zheng, T. Vazin, W. Yang, P. W. Goodwill, E. U. Saritas, L. R. Croft*, et al.*, "Quantitative Stem Cell Imaging with Magnetic Particle Imaging." *IEEE Xplore,* 2013.